RMetS
Royal Meteorological Society

Lagrangian overturning and the Madden–Julian Oscillation

Patrick Haertel[a]* Katherine Straub[b] and Alexey Fedorov[a]
[a]*Department of Geology and Geophysics, Yale University, New Haven, CT, USA*
[b]*Department of Earth and Environmental Sciences, Susquehanna University, Selinsgrove, PA, USA*

*Correspondence to: P. Haertel, Department of Geology and Geophysics, Yale University, 210 Whitney Avenue, New Haven, CT 06510, USA. E-mail: patrick.haertel@yale.edu

The Madden–Julian Oscillation (MJO), a planetary-scale disturbance in zonal winds and equatorial convection that dominates intraseasonal variability in the Tropics, is a challenge to explain and notoriously difficult to simulate with conventional climate models. This study discusses numerical experiments conducted with a novel Lagrangian atmospheric model (LAM) that produce surprisingly robust and realistic MJOs, even at very low resolution. The LAM represents an atmosphere as a collection of conforming air parcels with motions that are predicted using Newtonian mechanics. The model employs a unique convective parametrization, referred to as Lagrangian overturning (LO), in which air parcels exchange vertical positions in convectively unstable regions. A key model parameter for simulating MJOs is the mixing between adjacent ascending and descending parcels, with more frequent and stronger MJOs occurring when greater mixing is prescribed. Sensitivity tests suggest that MJOs simulated with the LAM are not particularly sensitive to model resolution, but their structure and propagation speed do depend on sea-surface temperatures, large-scale precipitation patterns and surface fluxes. An important conclusion of this article is that the most fundamental dynamics of the MJO are captured by the LO convective parametrization coupled with large-scale atmospheric circulations.

Key Words: Madden–Julian Oscillation; Lagrangian modeling; tropical convection.

Received 12 October 2012; Revised 13 June 2013; Accepted 17 June 2013; Published online in Wiley Online Library

1. Introduction

The Madden–Julian Oscillation (MJO) is a planetary-scale 30–60 day variation in zonal winds and moist convection that occurs near the Equator (Madden and Julian, 1971, 1972, 1995; Zhang, 2005). The region of active convection in the MJO typically propagates slowly eastward ($\sim$5 m s^{-1}; Weickman *et al.*, 1985) starting over the western Indian Ocean and diminishing just east of the International Date Line, and it includes smaller scale, higher frequency disturbances moving both eastward and westward (Hendon and Liebman, 1994; Nakazawa, 1998). An approaching MJO convective disturbance is preceded by easterly wind perturbations in the lower troposphere and westerly perturbations in the upper troposphere, as well as a gradual moistening of the lower troposphere that deepens with time; the wind perturbations then reverse and the troposphere dries out following the passage of the convective centre (Kiladis *et al.*, 2005). There have been many theories put forward to explain the genesis, propagation and structure of the MJO (e.g. see review by Wang, 2005), including radiative destabilization (Raymond, 2001), wind-induced surface heat exchange (Emanuel, 1987), the discharge–recharge hypothesis (Blade and Hartmann, 1993), wave-Conditional Instability of the Second Kind (CISK) (Lau and Peng, 1987), coupling with equatorial Rossby waves (Majda and Stechmann, 2009) and the characterization of the MJO as a moisture mode (e.g. Sobel and Maloney, 2012), but there is not yet a scientific consensus on what constitutes the most fundamental dynamics of the MJO.

Conventional climate models continue to struggle to properly represent the MJO, with inaccuracies in precipitation amplitude, eastward propagation and period (e.g. Lin *et al.*, 2006; Kim *et al.*, 2009, 2011). This deficiency of climate models is particularly troubling because the MJO has been shown to have global effects on weather and climate, impacting the El Nino Southern Oscillation (e.g. Kessler and Kleeman, 2000; Kessler, 2001; Fedorov, 2002; Federov *et al.*, 2003), tropical cyclone formation (Maloney and Hartmann, 2000; Barrett and Leslie, 2009), Asian and North American monsoons (Wu *et al.*, 1999; Lorenz and Hartmann, 2006), and even high-latitude weather (Vecchi and Bond, 2003; Cassou, 2008). While there are many possible causes for poor simulations of MJOs, recent success in simulating MJOs with the cloud-resolving or 'super' convective parametrization (e.g. Grabowski, 2001; Khairoutdinow *et al.*, 2001; Thayer-Calder and Randall, 2009) suggest that conventional cumulus parametrizations might lack physics fundamental to the MJO.

In this study it is shown that a Lagrangian framework for fluid modeling and convective parametrization has advantages for simulating MJOs. A recently developed Lagrangian atmospheric model (LAM; Haertel and Straub, 2010) is used to simulate atmospheric circulations on an aquaplanet with realistic

© 2013 Royal Meteorological Society

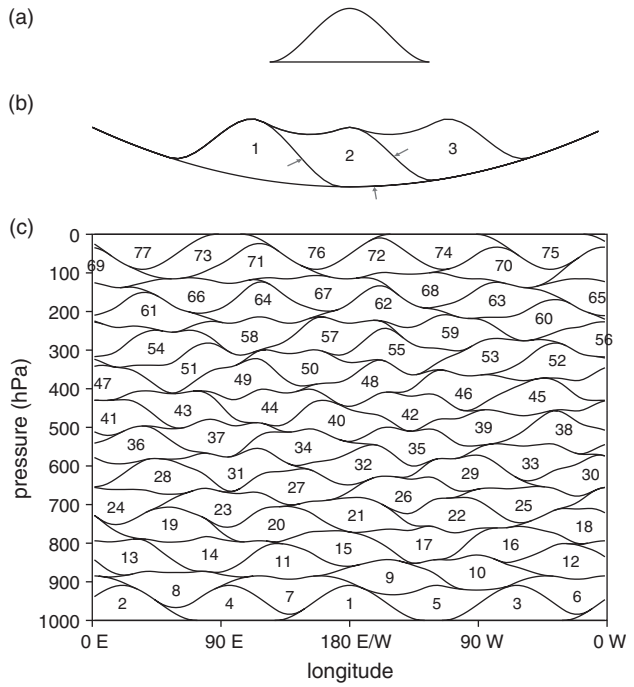

Figure 1. The conforming parcel concept. (a) The vertical thickness distribution for a single parcel. (b) Three parcels on the lower boundary with arrows indicating pressure forces on Parcel 2 (from Haertel, 2012). (c) An atmosphere comprising 77 parcels numbered according to their stacking order. These illustrations are drawn for large, two-dimensional parcels for simplicity and clarity; however, in the Lagrangian atmospheric model parcels are smaller and three-dimensional, with much more complicated patterns of interfaces between parcels (i.e. resembling spaghetti diagrams).

prescribed sea-surface temperatures (SSTs). The model employs a unique convective parametrization, referred to as Lagrangian Overturning (LO), in which air parcels exchange vertical positions in convectively unstable regions. When a moderate amount of mixing is prescribed between adjacent ascending and descending parcels, which mimics the effects of convective entrainment and detrainment, robust MJOs spontaneously form and have realistic structure, propagation and locations of formation and dissipation. Sensitivity tests suggest that MJOs simulated with the LAM are not particularly sensitive to model resolution, but their structure and propagation speed do depend on SSTs, large-scale precipitation patterns and surface fluxes.

This study is organized as follows. Section 2 describes the LAM. In Section 3 we compare MJOs simulated with the LAM to observed MJOs. Section 4 discusses the sensitivity of MJO structure and propagation to mixing, SST patterns, surface fluxes and radiation. Section 5 explores how MJOs change as model resolution in increased. Section 6 discusses the relationship between MJO activity and equatorial super rotation. Section 7 is a summary and discussion.

2. Lagrangian atmospheric model

The LAM simulates atmospheric circulations by predicting motions of individual air parcels. It was created by modifying a Lagrangian ocean model also based on a parcel concept (Haertel and Randall, 2002; Haertel and Straub, 2010; Haertel, 2012). This section reviews key features of the LAM including the conforming parcel concept and equations of motion, and introduces several new column physics packages, which are implemented for this study.

2.1. Conforming air parcels

The LAM represents an atmosphere as a collection of air parcels, each of which has the same bell-shaped vertical thickness distribution (Figure 1(a)):

$$dp(x', y') = dp_{\max} s\left(\frac{|x'|}{r_x}\right) s\left(\frac{|y'|}{r_y}\right) \tag{1}$$

where $dp_{\max}$ is the parcel's maximum vertical thickness in units of pressure, r_x and r_y are the parcel radii in the x and y directions (which are the same for each parcel), the prime ($'$) notation denotes a coordinate system centred on the Parcels', and $s(r) = 1 + (2r-3)r^2$ for $r < 1$. Parcels surfaces conform (i.e. there are no vertical gaps between overlapping parcels), so that the pressure at the upper surface of a given parcel at a given location is obtained by summing the pressure thicknesses of all parcels above it at that location. Figure 1(b) illustrates how parcels exert pressure on one another; in this case the lower boundary pushes upward and to the left on Parcel 2, Parcel 1 pushes upward and toward the right on Parcel 2, and Parcel 3 pushes downward and toward the left of Parcel 2. There is a ranking of parcels referred to as the stacking order, and parcels with a lower rank lie beneath parcels with a higher rank. Figure 1(c) shows a two-dimensional atmosphere comprising 77 parcels, with each parcel labelled according to its rank in the stacking order. Note that because parcels overlap one another to varying degrees, there is not a precise relationship between the parcel radius and the width of a grid box in a Eulerian model. Our experience has been that the equivalent Eulerian horizontal grid spacing is less than the Parcel radius, but that the equivalent Eulerian vertical grid spacing is greater than $dp_{\max}$ (i.e. that a layer a few parcels thick behaves like a single level in an Eulerian model).

2.2. Equations of motion

The equations of motion for a single air parcel are as follows:

$$\frac{\mathrm{d}\mathbf{x}}{\mathrm{d}t} = \mathbf{v} \tag{2}$$

$$\frac{\mathrm{d}\mathbf{v}}{\mathrm{d}t} + f\mathbf{k} \times \mathbf{v} = \mathbf{A}_\mathrm{p} + \mathbf{A}_\mathrm{m} \tag{3}$$

where $\mathbf{x}$ is horizontal position, t is time, $\mathbf{v}$ is horizontal velocity, f is the Coriolis parameter, $\mathbf{k}$ is the unit vector in the vertical, $\mathbf{A}_\mathrm{p}$ is the horizontal acceleration of the parcel resulting from pressure, and $\mathbf{A}_\mathrm{m}$ is the horizontal acceleration from parameterized turbulent mixing of momentum. The pressure acceleration $\mathbf{A}_\mathrm{p}$ results from the net force of pressure integrated over the surface of the parcel (Haertel and Straub, 2010). The turbulent drag $\mathbf{A}_\mathrm{m}$ is implemented by allowing parcels to exchange momentum with their nearest neighbours (e.g. Haertel *et al.*, 2004, 2009). Parcels' horizontal positions and accelerations are explicitly predicted, but vertical positions are implicitly determined by the parcel stacking order (Figure 1(c)). For example, a parcel ascends when it rides up and over a ridge in bottom topography or other parcels, or when parcels converge beneath it.

2.3. Global Lagrangian overturning convective parametrization

The LAM includes a unique convective parametrization referred to as Lagrangian overturning, in which air parcels in convectively unstable regions exchange vertical positions. There are several ways the LO concept can be implemented in a Lagrangian model. For this study we use a different version of LO than that described by Haertel and Straub (2010; hereafter HS10). The version of LO used by HS10 (hereafter local Lagrangian overturning or LLO) involves comparing potential temperatures of pairs of parcels and swapping their vertical positions when doing so yields a greater potential temperature for the rising parcel. Here, we use a global sort of the parcel stacking order by potential temperature, and therefore refer to this version of LO as global Lagrangian overturning (GLO). The reason we elected to use GLO instead of LLO for this study is that when LLO is used as a convective

© 2013 Royal Meteorological Society

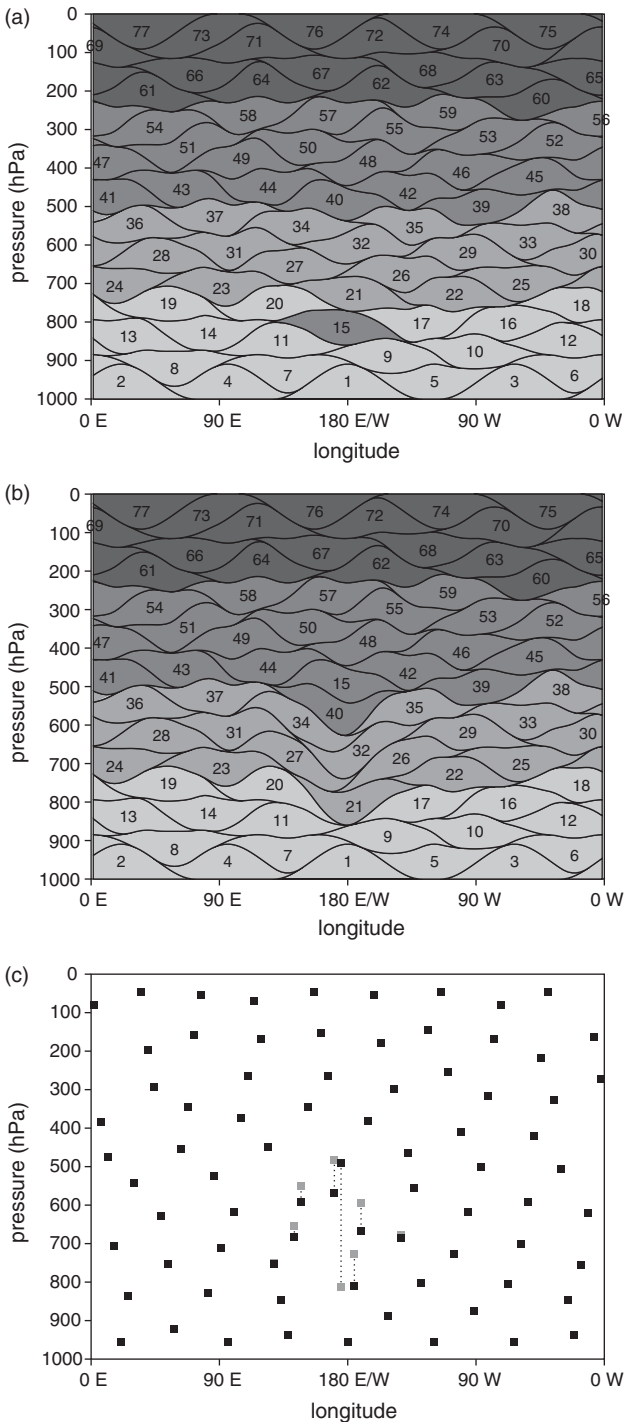

Figure 2. The global Lagrangian overturning convective parametrization. (a) Diabatic effects cause Parcel 15 to become warmer than nearby parcels (darker shades denote higher potential temperatures). (b) It ascends to its level of neutral buoyancy. (c) The resulting (black) and previous (grey) positions of parcel centres are shown with boxes, which illustrates the vertical displacements of the rising parcel and nearby parcels subsiding around it.

parametrization, a periodic global sort of parcel positions by potential temperature is still necessary. It turns out that model solutions, and MJO behaviour in particular, depend on the relative frequency of LLO and global sorts – a numerical side effect that does not occur when GLO is used exclusively as the convective parametrization.

Figure 2 illustrates the GLO for an idealized, two-dimensional atmosphere. Suppose that within a mostly stratified atmosphere diabatic effects cause an air parcel to be warmer than surrounding parcels (Figure 2(a)). The GLO parametrization redefines the parcel stacking order, so that the parcel in question rises to its level of neutral bouyancy as determined by its potential temperature (Figure 2(b)). The resulting vertical displacements of parcels are easy to discern when positions of parcel centres are shown both before (as grey boxes) and after (as black boxes) the overturning of air parcels (Figure 2(c)). In this case Parcel 15 rises several 100 hPa, and several nearby parcels subside on the order of 100 hPa or less. The net result is that the localized warming is spread out in the vertical direction, which is evident in the downward displacement of isentropes below Parcel 15 in Figure 2(b).

For simplicity, the GLO and condensation of water vapour are carried out as independent steps. In other words, first parcels ascend or descend to their level of neutral bouyancy as determined by their potential temperature, and then excess water condenses in saturated rising parcels (SRPs). This leaves a SRP in a state warmer than its environment at the end of the time step (e.g. Figure 2(a)), which is consistent with the behaviour of convective cells in nature (i.e. as a warm bubble rises it maintains a temperature greater than that of its environment). Typically, vertical displacements in a single time step are much lower that that shown schematically owing to a higher vertical resolution, and parcels take a dozen or more time steps to ascend within a deep updraft. In practice, the majority of the parcels in a column descend slowly while a few parcels ascend rapidly (e.g. Figure 2(c)), which is also consistent with air parcel behaviour in nature in convecting regions. However, some parcels in convecting regions also descend rapidly owing to effects of evaporative cooling, as in convective and stratiform downdrafts.

Non-entraining GLO (as defined above) is a fully Lagrangian process that does not require the use of a Eulerian grid. However, we do divide the model domain into columns (Figure 3(a)) in order to calculate mixing between rising and descending parcels, as well as evaporation of rain and cloud water. A parcel mixes with the parcels that it climbs past that are centred in the same column. For the overturning shown in Fig. 2, Parcel 15 mixes with Parcels 21, 32 and 40 (Figure 3(b)). For example, after Parcel 15 mixes with Parcel 21, the new value of potential temperature is:

$$\theta'_{15} = (1-\mu dp)\theta_{15} + \mu dp\theta_{21} \tag{4}$$

where μ is the prescribed convective mixing rate (given as a ratio per unit of pressure ascent) and dp is total pressure ascent of the rising parcel divided by the number of parcels it passes during the time step (in this case three). This formula is derived from the assumption that the rising parcel (15) and the parcel it passes (21) exchange mass, and the mixing of moisture and momentum is implemented in the same way. Note that the mixing occurs only when one parcel passes another in the column (i.e. vertical advection without overturning generates no mixing), and that the mixing is not dependent on the presence of liquid water.

For all of the simulations presented in this article, the horizontal extents of parcels in the LAM are orders of magnitude greater than those of convective cells in nature. However, our simulations reveal that rearranging the vertical positions of a few large parcels and mixing them according to the above rules captures the net effects of vertical transports and mixing by the many convective plumes in nature – as measured by mean profiles of moisture and temperature, precipitation patterns and convective system organization. We typically define the GLO column width to be smaller than the parcel radius by a factor of 1.5–3, which yields higher resolution of precipitation features, and leads to a more realistic zonal wind field.

2.4. *Precipitation*

Condensed water is converted to cloud water, and cloud water exceeding 1 g kg^{-1} is converted to rain. Rain falls one parcel down in the column per time step, evaporating at a constant rate per unit of pressure descent (within subsaturated parcels). Defining the evaporation in this way makes the total amount of evaporation to be relatively insensitive to the model time step.

© 2013 Royal Meteorological Society

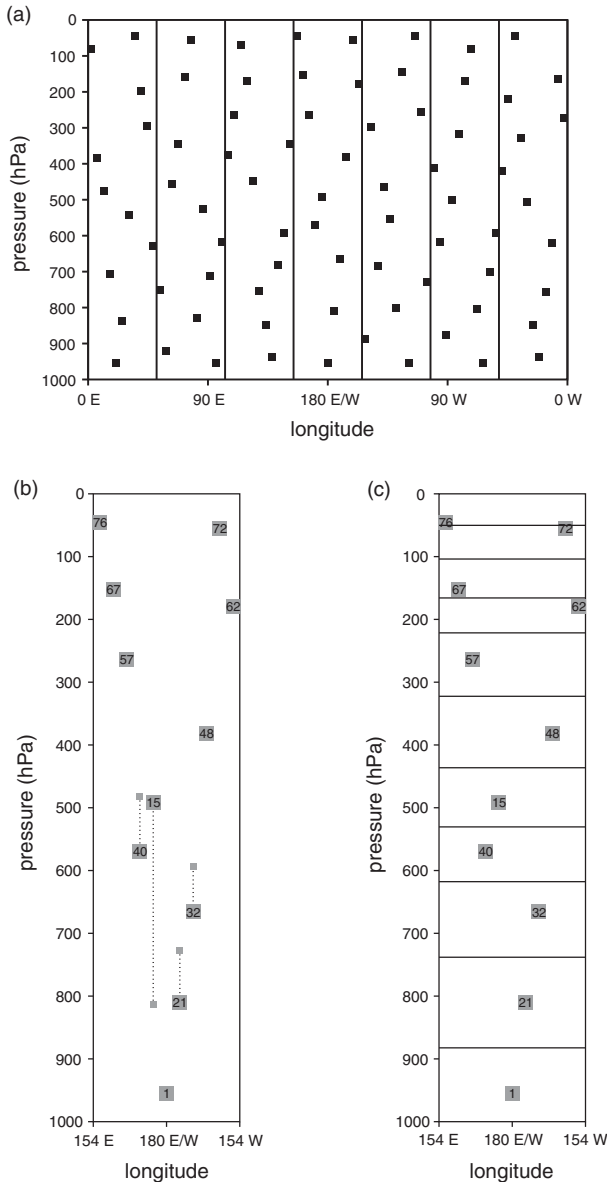

Figure 3. The geomeotry used for convective mixing and microphysics in the Lagrangian atmospheric model. (a) The model domain is divided into columns, and parcel centres are treated like grid points in a column of a Eulerian model. (b) The convective mixing between parcels is applied when parcels pass each other in a column; in this case Parcel 15 mixes with Parcels 21, 32 and 40 as it ascends in the column. (c) Each parcel centre has a vertical extent (dp) that extends halfway to the next parcel above and below it, this value of dp is used in calculating radiative heating and evaporation.

Figure 3(c) illustrates how the vertical extent of a parcel (dp) is defined for the purpose of calculating the evaporation of rain and cloud water in a time step.

2.5. *Surface fluxes*

Surface fluxes of latent heat and sensible heat have the form $F = C\Delta$ where C is a turbulent exchange coefficient and Δ denotes a difference between variables across the water–air interface (e.g. specific humidity, potential temperature). Turbulent exchange coefficients depend linearly on wind speed, and are calculated by a least squares fit of wind speed and heat flux data collected within the Coupled Ocean Atmosphere Response Experiment Intensive Flux Array (COARE IFA; Ciesielski *et al.*, 2003).

2.6. *Radiation*

The LAM's radiation scheme is a modified version of that described by Frierson *et al.*(2006), and the reader is referred to that study for details on the radiative transfer equations and the overall

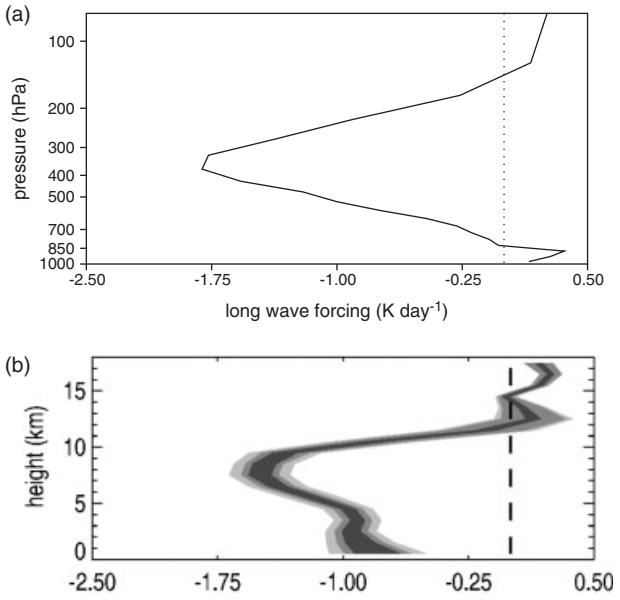

Figure 4. Vertical structure of net radiative forcing over the western Pacific warm pool in (a) a Lagrangian atmospheric model (LAM) simulation with the new radiation scheme and (b) estimates from L'Ecuyer and McGarragh (2010). Note that the LAM includes only long-wave forcing, with a reduction in the total radiative flux to account for the lack of short-wave forcing, whereas the observed profile includes both long-wave and short-wave forcing. The parameters for the radiation scheme in the LAM are tuned to make the altitude of the peak cooling and overall amplitude similar to those observed in nature.

framework of the scheme. Three modifications to the Frierson *et al.*scheme are used for this study: (i) a moisture-dependent equation for total optical depth, (ii) a modified vertical-structure function for optical depth, and (iii) and a reduction in the total radiative flux.

Our new equation for total optical depth is as follows:

$$\tau_0 = \tau_{0\mathrm{b}} + \tau_{0\mathrm{w}} \left(\frac{W}{40\ \mathrm{mm}} \right) \tag{5}$$

where τ_0 is the total optical depth, $\tau_{0\mathrm{b}}$ is the baseline optical depth, $\tau_{0\mathrm{w}}$ represents the sensitivity of optical depth to atmospheric moisture, and W is the precipitable water in millimetres The new vertical structure function has the form

$$\tau = \tau_0 \left(\frac{p}{p_0} \right)^n \tag{6}$$

where p is pressure, p_0 is the surface pressure and n is an integer. For the purposes of calculating radiative fluxes we use:

$$B = \mu \sigma T^4 \tag{7}$$

where B is the radiative flux, σ is the Stefan-Boltzman constant, and μ is used to reduce the intensity of the radiative cooling to account for the lack of short-wave forcing in the model and for regions of the infrared spectra in which there is little absorption or emission (i.e. atmospheric windows).

All parameters are tuned simultaneously to generate as realistically as possible thevertical structure and amplitude for radiative cooling in this simple framework. The values used for the simulations presented below are $\tau_{0\mathrm{b}} = 3$, $\tau_{0\mathrm{w}} = 7$, $n = 2$ and $\mu = 0.5$. Figure 4 compares the net radiative forcing in the model over the western Pacific warm pool to that estimated by L'Ecuyer and McGarragh (2010). Note that the model produces a peak cooling at the same height as the observationally based estimate, and that the overall amplitude of the radiative cooling is also similar. We use a more gradual taper of optical depth with height ($n = 2$) than that used by Frierson *et al.*(2006) to achieve this realistic vertical structure, which is consistent with the idea that not only water vapour but also cloud particles and other greenhouse gases make important contributions to long-wave optical depth.

© 2013 Royal Meteorological Society

2.7. Summary of new features

The following is a list of changes made to the LAM since it was introduced by Haertel and Straub (2010): (i) GLO replaces LLO as the convective parametrization; (ii) convective mixing and evaporation rates are now prescribed as ratios per unit of pressure ascent/descent, which makes total mixing and evaporation relatively insensitive to parcel thickness and time step; (iii) cloud water is included as a prognostic variable; (iv) a modified version of the Frierson *et al.*(2006) scheme is used for radiation; (v) surface fluxes depend on turbulent exchange coefficients fit to COARE data; (vi) a modified leapfrog time differencing replaces third-order Adams–Bashforth time differencing and allows a longer time step (i.e. greater computational efficiency); (vii) a Mercator projection is used in place of the spherical geometry described by Haertel *et al.*(2004), which is more numerically stable with the new time differencing and also more computationally efficient.

3. Simulated and observed MJOs

In this section we compare MJOs simulated with the LAM to those observed in nature. We examine MJO precipitation patterns, horizontal flow structures and vertical structures of wind, temperature and moisture. Despite the course resolution of the model, there is excellent agreement between simulated and observed MJOs, supporting the idea that the GLO convective parametrization and large-scale circulations capture the most fundamental dynamics of the MJO.

3.1. Model configuration

The LAM is run in an aquaplanet configuration, with prescribed SSTs from the World Ocean Atlas 2005 annual climatological mean temperature data set. Zonal mean SST values are used over continental locations. The model domain extends from 75°S to 75°N at the surface, with an increasing meridional extent with height (the numerics of the LAM require horizontal boundaries to have some slant, typically over a distance on the order of a parcel radius). The simulation is run for 1 year, starting with a dry isentropic atmosphere ($\theta = 302.5$ K).

The model uses rather wide but vertically thin parcels, with radii of 30° in longitude and 15° in latitude, and a maximum pressure thickness of 6.5 hPa. However, as is noted above, our experience has been that the equivalent horizontal grid spacing in a Eulerian model is one to three times lower than the parcel radius, and the equivalent vertical grid spacing is one to nine times higher than the maximum parcel vertical thickness. In other words, a layer several parcels thick with staggered parcel centres tends to behave like a single level in a Eulerian model. Moreover, as is shown below, MJO structure is not strongly sensitive to increases in resolution, except in cases where increasing resolution significantly alters the basic state precipitation pattern.

The columns used for parcel mixing, precipitation microphysics and radiation have a zonal width of 20°, a meridional extent of 5° and contain an average of 34 parcel centres per column. Other model parameters are listed in Table 1.

3.2. Rainfall time series

A time–longitude series of equatorial precipitation for the LAM simulation reveals a strong, cyclical MJO (Figure 5(a)). As in nature, convection intensifies over the Indian Ocean, propagates eastward at around 6 m s^{-1} and dissipates just east of the

Table 1. Model parameters for the control run.

Parcels	Columns	Mixing	Evaporation	Time step
30° × 15° × 6.5 hPa	20° × 5°	21×10^{-6} Pa^{-1}	12×10^{-6} Pa^{-1}	2400 s

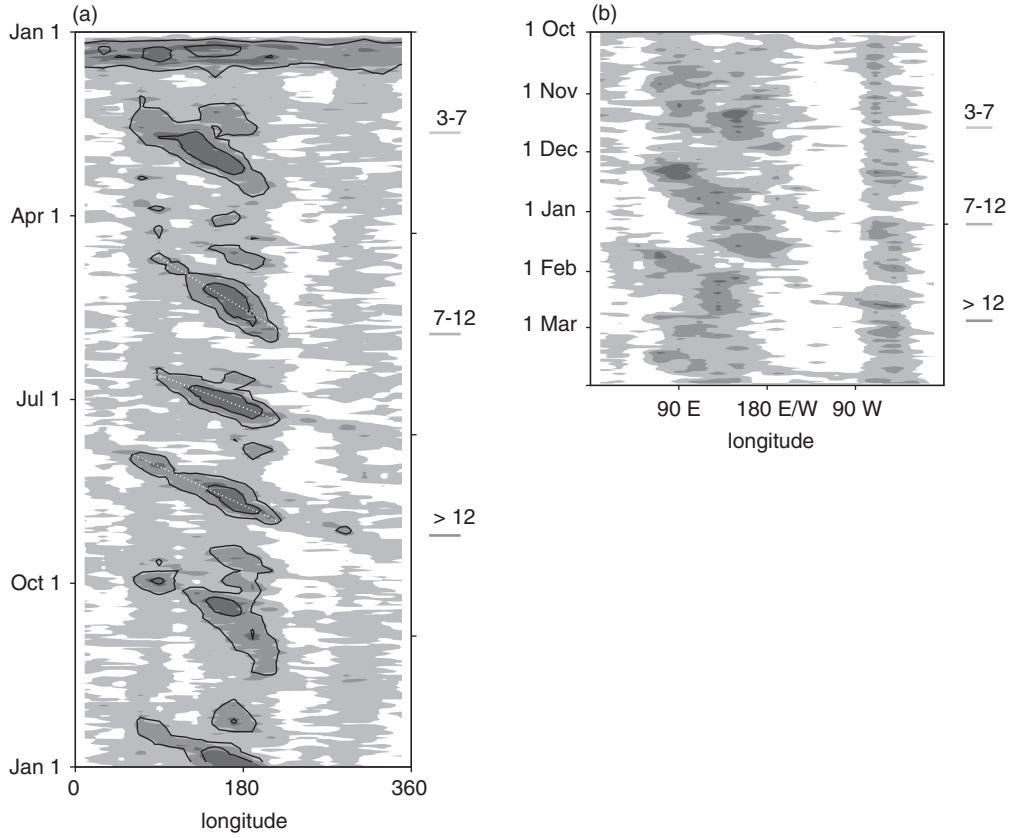

Figure 5. (a) Time–longitude series of rainfall (shading) for a Lagrangian atmospheric model (LAM) simulation with a series of Madden–Julian Oscillations (MJOs), with contours of low-pass filtered rainfall shown for 7 and 12 mm day^{-1}. Dotted lines trace out approximate paths of MJOs, and are used to construct composite vertical and horizontal structures shown in the following figures. The average phase speed is 5.9 m s^{-1}. (b) Observed time series of rainfall (Global Precipitation Climatology Project) for a series of MJOs that occurred between October 2007 and March 2008 with a resolution reduced to that of the LAM simulation.

© 2013 Royal Meteorological Society

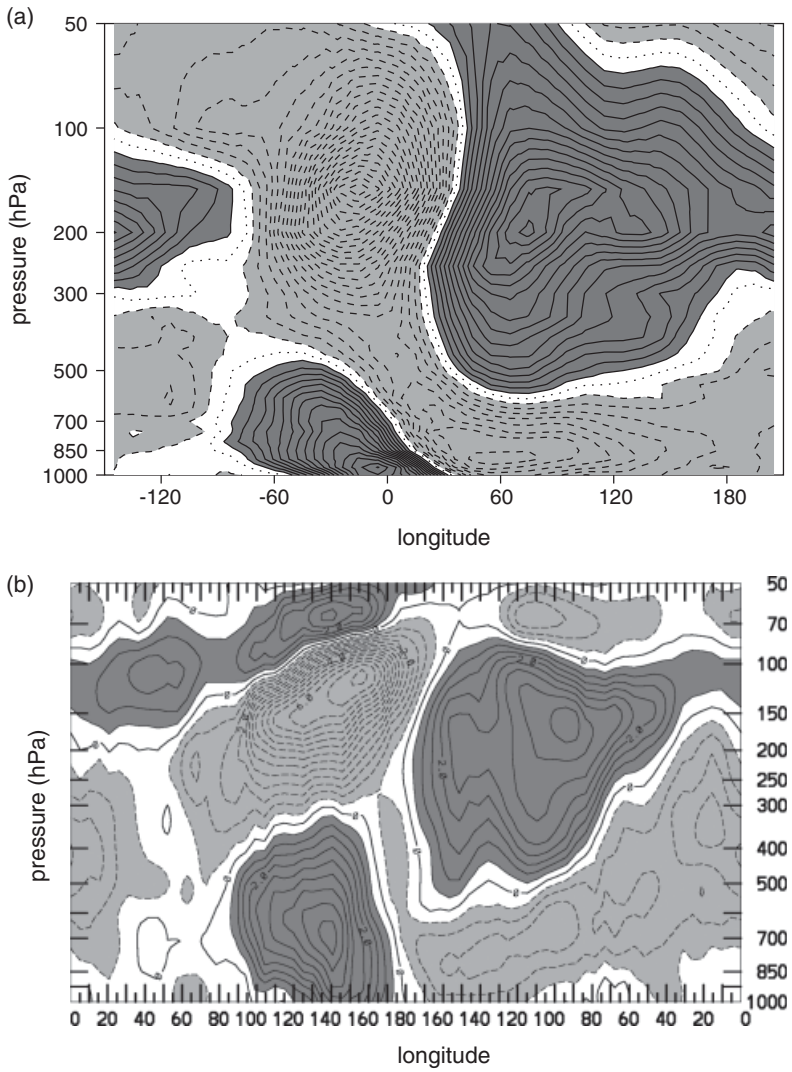

Figure 6. Composite vertical structure of zonal wind (0.5 m s^{-1} contour interval) for (a) simulated and (b) observed Madden–Julian Oscillations. The observed structure is taken from Kiladis *et al.* (2005).

International Date Line (Figure 5(a) and (b)). The period of the disturbance is roughly 50 days (Figure 5(a)), which is also consistent with observations. The simulated MJO (Figure 5(a)) is actually more regular and intense then that observed in nature (e.g. Figure 5(b)), which is a consequence of our selecting an MJO favourable parameter regime for this simulation (see parameter sensitivity tests below).

3.3. *Vertical structure*

In Figure 6(a) we show a composite MJO zonal wind structure (for the three MJOs marked with dotted lines in Figure 5(a)), which was constructed by computing a time average in a coordinate system moving with the MJO precipitation centre. Ahead of the most intense convection (i.e. for positive longitudes) there is a broad region of lower tropospheric easterlies, and trailing the precipitation a more narrow area of lower tropospheric westerlies that tilts westward with height (Figure 6(a)). Upper tropospheric flow is out of phase with lower tropospheric flow, and the lower tropospheric easterlies are connected with the upper tropospheric easterlies in a narrow region near the precipitation centre. Lower tropospheric easterlies also rise with height towards the east, and eventually connect with upper tropospheric easterlies after wrapping around the globe, but with a gap in the strong easterles to the west and above the low-level westerlies (Figure 6(a)). Although there are some differences between the simulated and observed zonal winds (e.g. deeper low-level westerlies in the observations), the features we mention above are shared in common with both simulated and observed MJOs (Figure 6).

The most prominant temperature feature is an upper-level warm anomaly peaking between 300 and 400 hPa near the precipitation centre that tilts downward toward the east (Figure 7(a)), with cooler air above, to the west and beneath it. The positive temperature anomaly also extends upward and to the east in a ridge, with a weak negative temperature anomaly near 300 hPa roughly 100° to the east of the precipitation centre (Figure 7(a)). Once again, most of the simulated features are also present in the observed MJO (Figure 7(b)), with a few notable differences near the surface to the west of the precipitation centre.

A low-level moist anomaly develops ahead of the simulated MJO, which transitions to a deep and intense moisture anomaly accompanying the heaviest rainfall, which is followed by deep tropospheric dryness (Figure 8(a)). The deep moist and dry anomalies tilt slightly to the west with height. The observed MJO exhibits this same structure, but with a somewhat deeper moisture anomaly to the east of the precipitation centre (Figure 8(b)).

Overall, the gross vertical structures of wind, temperature and moisture are consistent with those observed by Kiladis *et al.*(2005), with a few minor differences attributable to the idealized nature of the simulations and their course resolution (see below).

3.4. *Horizontal structure*

The 850 hPa horizontal flow includes a pair of cyclonic gyres that straddle the Equator to the west of the precipitation centre, and which are associated with westerlies that flow into the most intense convection (Figure 9(a)). To the east of these gyres

© 2013 Royal Meteorological Society

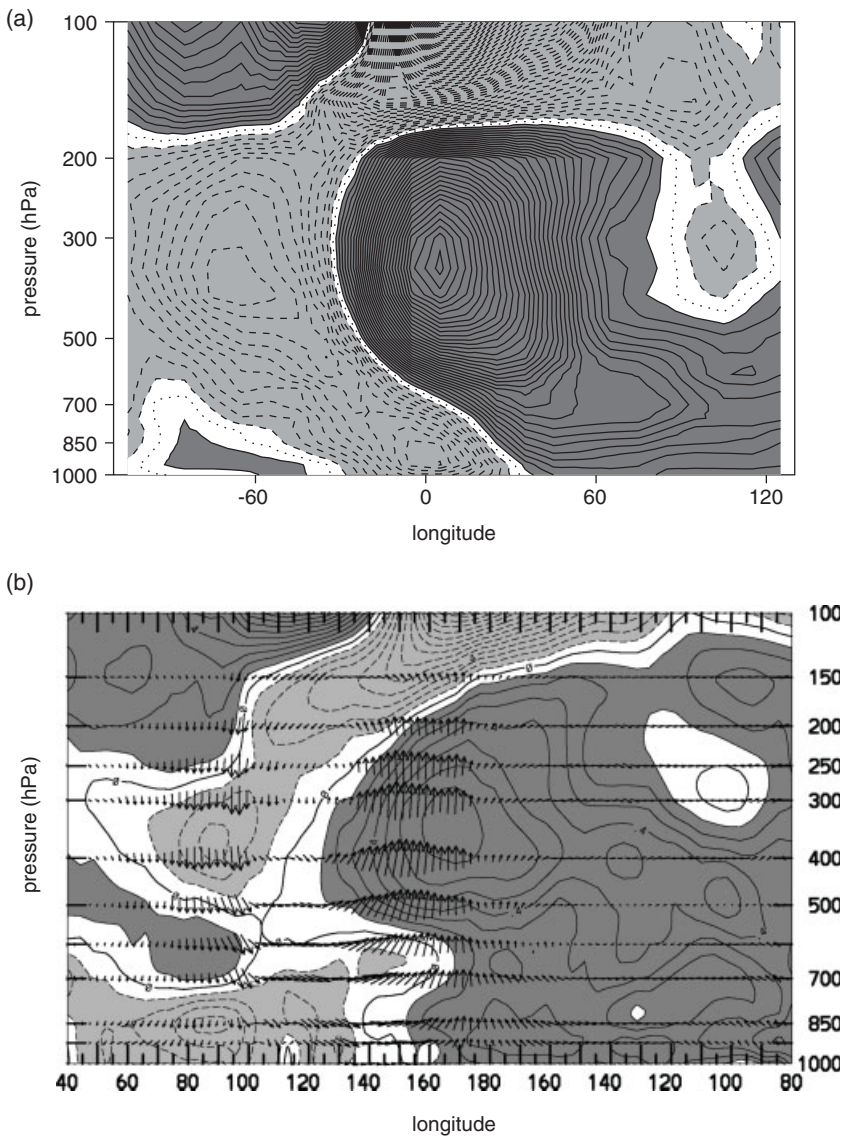

Figure 7. Composite vertical structure of temperature perturbations (0.1 K contour interval) for (a) simulated and (b) observed Madden–Julian Oscillations (MJOs). The observed structure is taken from Kiladis *et al.*(2005). Note that potential temperature perturbations are plotted for the Lagrangian atmospheric model (LAM), whereas *in situ* temperature perturbations are shown for the observed MJO, which contributes to the higher amplitudes seen in the LAM.

there are broader anticyclonic gyres, accompanied by a long fetch of equatorial easterlies. The observed 850 hPa composite shows a similar flow pattern and positioning of gyres relative to precipitation patterns (Figure 9(b))

At 200 hPa there is a classic quadrapole gyre, with a pair of anticyclone gyres just to the west and poleward of the precipitation centre, and a pair of cyclonic gyres on either side of the Equator much further to the east (Figure 10(a)). To the west of the precipitation centre the easterly flow diverges from the Equator, and to the east of the precipitation centre there is meridional convergence. Once again these key flow features are also present in the observed MJO, with a similar positioning relative to the precipation centre (Figure 10(b)).

The numerous realistic aspects of the simulated MJOs, including their period, location of origin and dissipation, rate of propagation, vertical structures of zonal wind, temperature and moisture, as well as horizontal flow structures at low and upper levels, all provide evidence that the course resolution LAM coupled with the GLO convective parametrization captures the most fundamental dynamics of the MJO, a point that we will return to in section 7.

3.5. *Basic state*

An examination of average rainfall patterns, zonal winds and profiles of moisture and temperature reveal that the simulated MJOs occur in a fairly realistic basic state, especially considering the idealized nature and course resolution of the simulation.

Figure 11(a) shows the average rainfall for days 100–365 of the MJO simulation (excluding a 100 day spin-up period). As in the Global Precipitation Climatology Project (GPCP; Huffman *et al.*, 2001) observed annual rainfall map (Figure 11(b)), there is a region of heavy rainfall straddling the Equator from the eastern Indian Ocean to just east of the Dateline. There is also an intertropical convergence zone (ITCZ) extending eastward over the eastern Pacific, across what would be South America (if the model had continents), and into the Atlantic. The simulation exhibits no evidence of an unrealistic heavy rain band from 10° to 20°N between 60° and 160°E , which has been found in conventional climate models tuned to have strong MJOs (Kim *et al.*, 2011).

Figure 12(a) shows average zonal winds for the LAM simulation. At low levels the winds are similar to those observed in nature: there are weak easterlies from about 30°S to 30°N that peak slightly above 5 m s^{-1} near the surface around 15°N/S, and westerlies that increase in amplitude with height at midlatitudes (Figure 12(a)). Simulated upper-level midlatitude zonal jets are also similar to observed jets, with maximum amplitudes between 25 and 35 m s^{-1} located near 200 hPa (Figure 12(a) and (b)). However, one feature of the LAM simulation that is noticeably different from observations is the presence of westerlies or super rotation in the upper troposphere over the Equator. Numerous

© 2013 Royal Meteorological Society

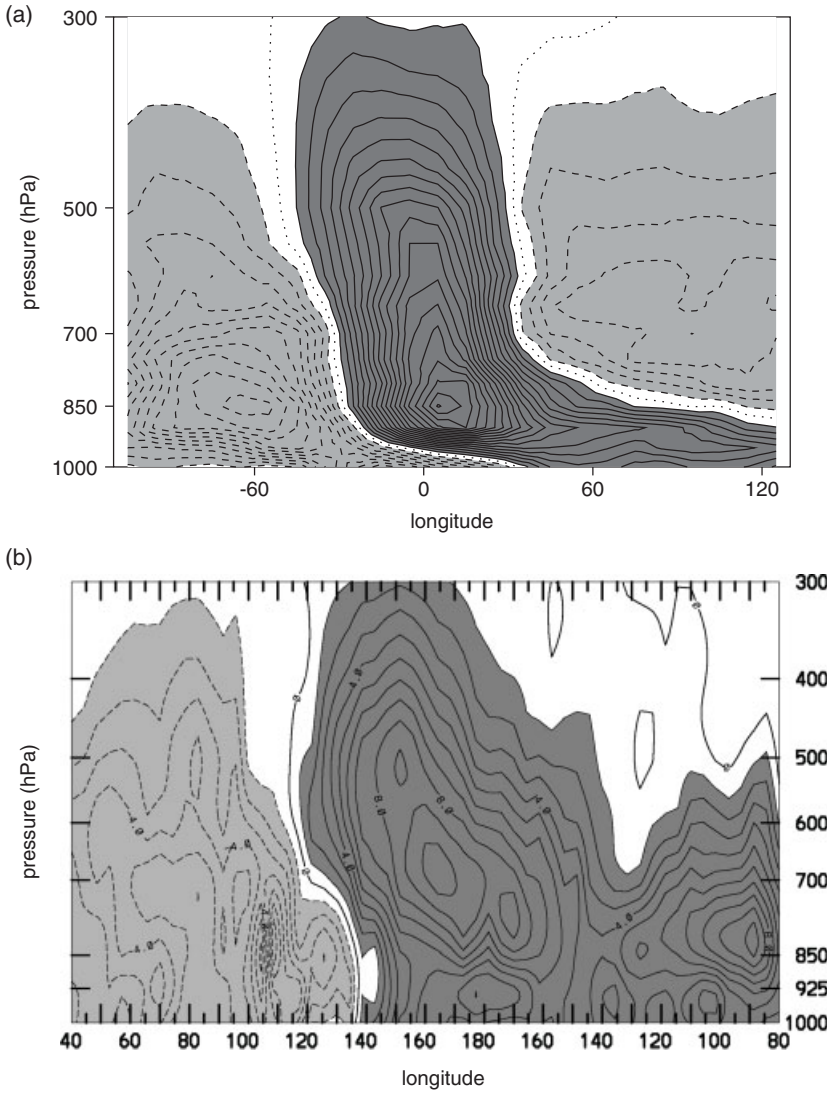

Figure 8. Composite vertical structure of specific humidity (0.1 g kg^{-1} contour interval) for (a) simulated and (b) observed Madden–Julian Oscillations. The observed structure is taken from Kiladis *et al.* (2005).

LAM simulations we have conducted suggest that there is a correlation between these westerlies and MJO activity, an issue that we discuss further in section 6.

The basic state in which the MJOs occur is also fairly realistic in terms of temperature and moisture profiles. Figure 13(a) shows that over the western Pacific warm pool, the simulated temperature is close to the observed temperature throughout the troposphere and into the lower stratosphere. The simulated temperature is slightly cooler in the upper troposphere and slightly warmer near the tropopause. The simulated moisture profile in this region is even more realistic (Figure 13(b)): it is within a fraction of 1 g kg^{-1} of the observed profile throughout the troposphere.

Hereafter we refer to the simulation presented in Figures 5–13 as the control simulation, because we perform numerous sensitivity tests using this simulation as a starting point.

4. Physical sensitivity tests

The simulations presented in this section, for which model parameters are listed in Table 2, help to identify how MJOs simulated with the LAM depend on physical parameters included in the model.

4.1. Mixing

It turns out that the most important model parameter for determining the existence and intensity of MJOs in the LAM is the mixing between ascending and descending parcels within the Lagrangian overturning convective parametrization. Reducing this parameter by roughly 20% from the control run causes the MJO to be slower and to have a greater period (Figure 14(a)). The MJO also becomes less robust in the sense that it can disappear when other model parameters are tweaked slightly in combination with this change (e.g. radiation, surface fluxes, evaporation of falling rain). However, the horizontal and vertical structures of composite MJOs are nearly identical to those for the control case (not shown). When the mixing parameter is further reduced to 4/7 the value in the control run (Figure 14(b)), there is still some sign of an MJO, but it is not nearly as realistic, with only weak variability over the Indian Ocean. Reducing the mixing parameter by a factor of three from the control case causes the MJO to disappear entirely (Figure 14(c)). This more extreme parameter change also makes the profile of temperature in the Tropics quite unrealistic, with simulated temperatures exceeding observed temperatures by more that 5 K in the upper troposphere. In other words, selecting a value of mixing between rising parcels and their environment that produces a realistic temperature profile also seems to generate a realistic MJO.

4.2. SST

When zonally symmetric SSTs (based on the Qobs case of Neale and Hoskins, 2000) are prescribed instead of climatological SSTs, a long-lived wavenumber 1 disturbance develops that circles the globe multiple times, before dividing into a wavenumber

© 2013 Royal Meteorological Society

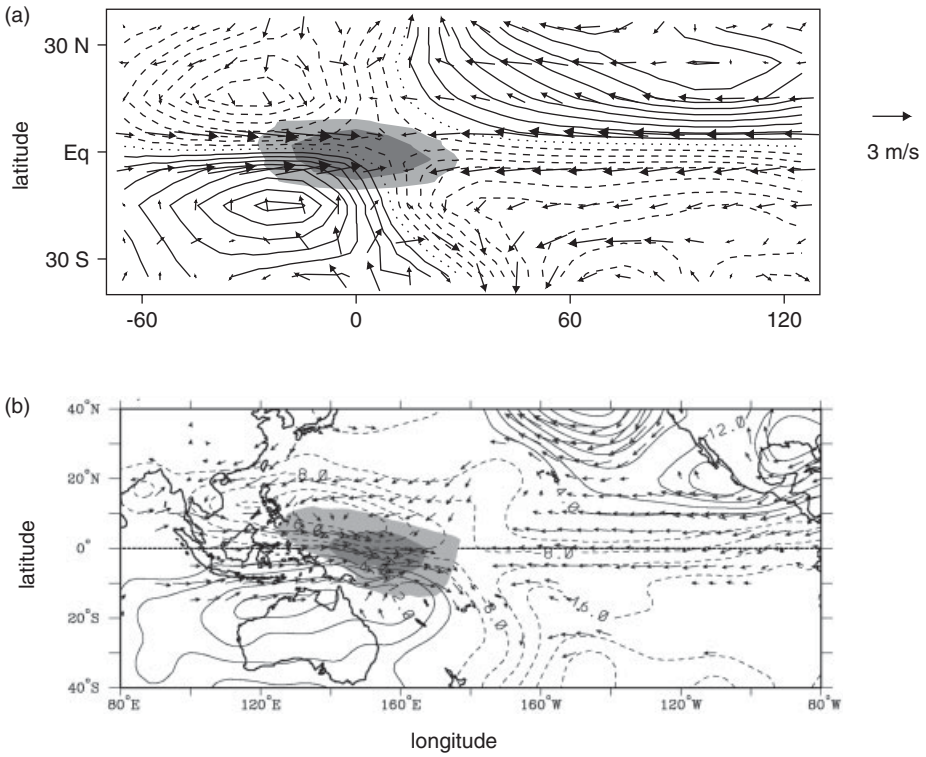

Figure 9. Composite horizontal structures of 850 hPa flow (4×10^5 m^{2}s^{-1} contour interval) for (a) simulated and (b) observed Madden–Julian Oscillations. The observed structure is taken from Kiladis *et al.*(2005). Regions of precipitation with values greater than 3 and 7 mm day^{-1} are shaded light and dark in (a) respectively. Outgoing long-wave perturbations of less than -16 and -32 W m^{-2} are shaded light and dark in (b) respectively.

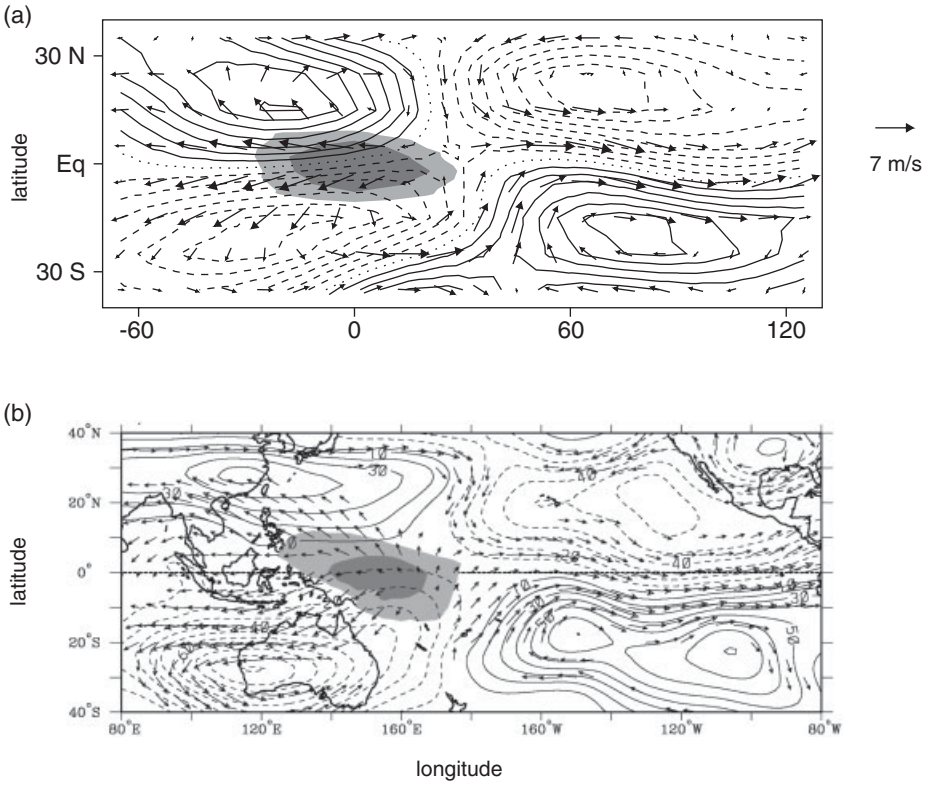

Figure 10. Composite horizontal structures of 200 hPa flow (10^6 m^{2}s^{-1} contour interval) for (a) simulated and (b) observed Madden–Julian Oscillations. The observed structure is taken from Kiladis *et al.*(2005). Regions of precipitation with values greater than 3 and 7 mm day^{-1} are shaded light and dark in (a) respectively. Outgoing long-wave perturbations of less than -16 and -32 W m^{-2} are shaded light and dark in (b) respectively.

2 disturbance several hundred days into the simulation (Figure 15(a)). The vertical and horizontal structures of the wavenumber 1 disturbance (e.g. Figure 15(b) and (c)) are consistent with those of the MJO in the control run and in observations (Figures 6–10). It propagates at an average speed of 8.7 m s^{-1}, which is a little faster than MJOs in the control run and in nature. However, we still consider this disturbance to be an MJO and not a Kelvin wave owing to its horizontal circulation pattern, which includes a quadrapole gyre with strong off-equatorial rotational flow and meridional convergence to the east of the precipitation centre and meridional divergence to its west (Figure 15(c)). The average rainfall pattern (Figure 15(d)) shows a narrow, zonally symmetric ITCZ centred on the Equator. We have found that in general, MJOs simulated with the LAM

© 2013 Royal Meteorological Society

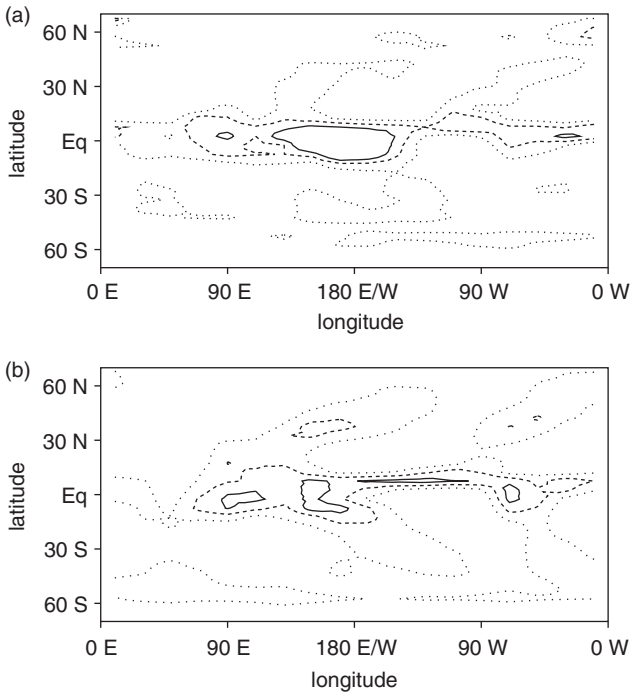

Figure 11. Average rainfall pattern. (a) Lagrangian atmospheric model simulation after initial spin-up (days 100–365). (b) Observed annual rainfall from the Global Precipitation Climatology Project data set for 1979–2010. For both panels 3, 5 and 7 mm day^{-1} contours are shown with dotted, dashed and solid lines respectively.

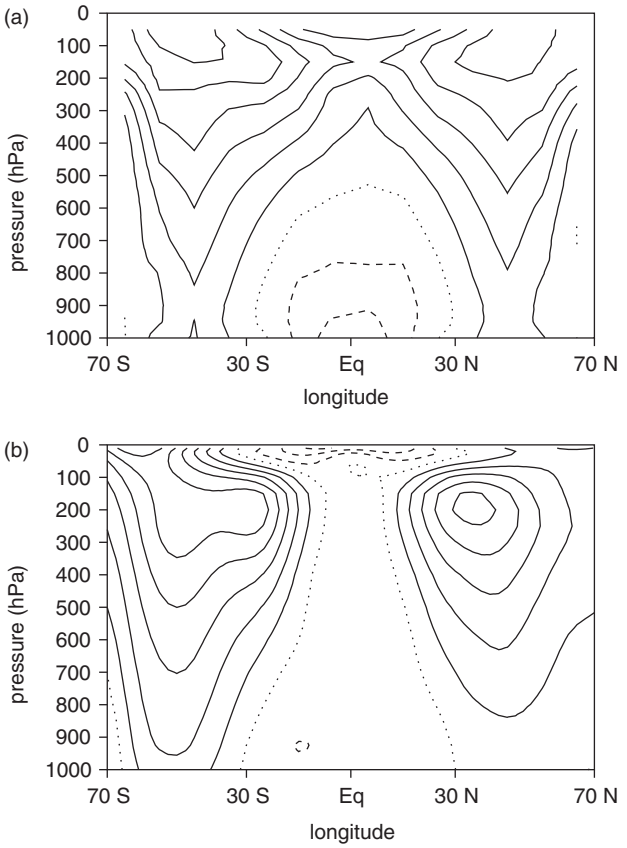

Figure 12. Average zonal wind (5 m s^{-1} contour interval). (a) Lagrangian atmospheric model (LAM) simulation with Madden–Julian Oscillations favourable model parameters (days 100–365). (b) Observed (NCEP-DOE Reanalysis 2 for the period 1979–2010). The LAM zonal wind averages are calculated by dividing the meridional domain into ten degree wide sections and averaging zonal velocities of parcels in each section.

propagate more quickly when the heaviest rainfall is confined in a narrow equatorial band.

One feature of the composite MJO zonal flow that is more realistic in this case than in the control run, is that the low-level easterlies to the east of the precipitation centre rise higher in the atmosphere (Figure 15(b)). This is typical for LAM runs in which there is some zonal wavenumber 2 structure in the precipitation field, as there is in this case, even when the wavenumber 1 structure is most pronounced in the middle of the year (Figure 15(a)).

We also conducted a run with a broader SST peak and a 1 K zonal wave number 1 SST perturbation (not shown). In this case a strong cyclical MJO develops that is most active over the warmer waters, much like in the control run. This result suggests that it is the gross structure of the SST pattern that determines the general behaviour of the MJO, including its regions of convective activity, propagation speed and period.

4.3. *Radiation*

One theory of the MJO is that a reduced long-wave cooling in the convectively active region contributes to its instability (Raymond, 2001). In order to test this concept for the LAM MJO, we modify our radiation scheme to be moisture insensitive by using the following equation for optical depth:

$$\tau_0 = \tau_{0b} + \mathrm{t}_{0l}(90^\circ - \varphi)/90^\circ \qquad (8)$$

where τ_{0l} is set equal to τ_{0w} (defined above) and ϕ is latitude. This yields a similar overall pattern to optical depth with high values near the Equator and low values near the Poles, but which is insensitive to local atmospheric water vapour variations (and more like the Frierson *et al.*, 2006 scheme). Figure 16 shows that MJOs with similar amplitudes, propagation speeds and horizontal and vertical structures develop with the 'grey' version of the radiation scheme. However, long-lived MJOs are less prevalent in this case, with some forming to the east of the Indian Ocean. This result suggests that although radiation instability is not necessary for the LAM MJO, it may enhance its instability and affect its region of formation.

4.4. *Wind-induced surface heat exchange*

Emanuel (1987) suggested that enhanced evaporation to the east of the MJO convective centre destabilizes the disturbance owing to the existence of basic state easterly winds in the Tropics, and the observed dependence of surface fluxes on wind speed. Although this idea has been questioned by subsequent studies that note that MJOs often occur in regions with basic state westerlies and that surface fluxes may actually weaken MJOs (e.g. Lin and Johnson, 1996; Haertel *et al.*, 2008), other more recent studies that characterize the MJO as a moisture mode also emphasize the importance of wind-dependent surface fluxes by enhancing evaporation in MJO *westerlies* (Sobel and Maloney, 2012). Such studies motivate an experiment with the LAM in which the wind-dependent nature of surface heat fluxes is turned off. For the purpose of calculating these fluxes, a constant surface wind speed of 5 m s^{-1} is assumed. Figure 17(a) shows the resulting time–longitude series of rainfall. The MJO continues to exist, with similar regions of formation and dissipation, propagation speeds, vertical and horizontal structures, but in this case it has a shorter horizontal wavelengh (i.e. wavenumber 2 structure), which also leads to a short period. This result suggests that wind-dependent surface fluxes are not necessary for the LAM MJOs, but they are a factor in selecting the preference for zonal wavenumber 1.

5. Numerical sensitivity tests

For the bulk of the simulations presented in this article we use a very low model resolution, which is sufficient for resolving planetary-scale circulations, but not all synoptic-scale circulations. As is mentioned above, the fact that the MJO can be simulated with such a low resolution is an important result in terms of what it implies about the dynamics of the MJO.

© 2013 Royal Meteorological Society

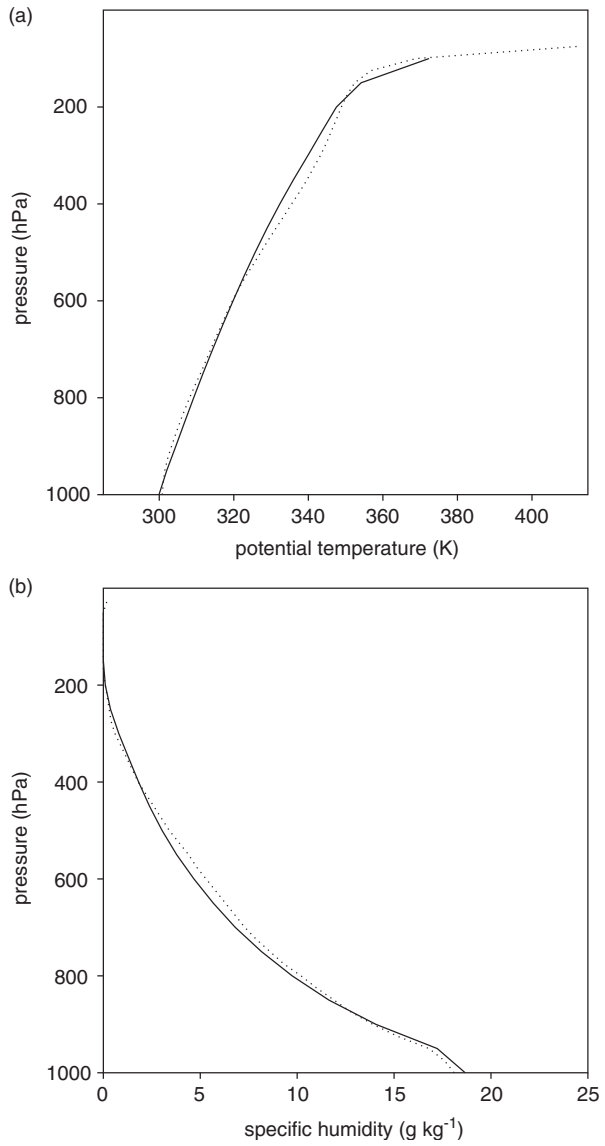

Figure 13. Vertical profiles of (a) temperature and (b) moisture over the western Pacific warm pool for the control simulation (solid) and COARE IFA (dashed).

Table 2. Model parameters for physical sensitivity tests.

Run(s)	Mixing (Pa^{-1})	SST	Radiation	Surface fluxes
1–3	$7, 12, 17 \times 10^{-6}$	Observed	Moisture dependent	Wind dependent
4	21×10^{-6}	Zonal symmetry	Moisture dependent	Wind dependent
5	21×10^{-6}	Observed	Moisture independent	Wind dependent
6	21×10^{-6}	Observed	Moisture dependent	Wind independent

Moreover, using this low resolution reduces the computational requirements of the numerous simulations needed to tune model parameters. However, it is also important to establish that the disturbances we identify as MJOs are not the result of some sort of parcel-scale numerical artefact. This section systematically explores the effects of changes in model resolution in time and space on both precipitation patterns and MJO structure. Parameters for the simulations in this section are listed in Table 3.

5.1. *Temporal resolution*

We performed experiments in which we halved the model time step for all model components, and also for just the column physics packages (e.g. GLO, radiation, surface fluxes). Each of these changes increases the fall speed of rain by a factor of two (because rain falls one parcel per time step in a column). However, the amount of evaporation in a given time step is dependent on the pressure *distance* the rain falls, and not time, a model attribute that is intended to decrease the LAM's sensitivity to time-step changes. In both time-step reduction experiments MJOs develop that are quite similar to those in the control case. For example, Figure 18(a) shows the results of reducing the time step of column physics. A series of MJOs forms with similar amplitudes, propagation speeds and regions of formation and dissipation to those in the control case. Their vertical and horizontal structures are also similar, as is the overall rainfall pattern (not shown).

5.2. *Vertical resolution*

We also performed experiments in which we altered the vertical resolution of the model. This is not a purely a numerical modification, as it changes the number of parcels in a column, which has the potential to change the ratio of ascending to descending parcels (i.e. updraft areal coverage), as well as the amplitude and vertical penetration of surface fluxes. Nevertheless, the MJO is present with both reductions and increases in the vertical thickness of parcels. For example, Figure 18(b) shows the results of a simulation in which the vertical thickness (number) of parcels is increased (decreased) by 30%. Not only is the MJO present in this case, but it is also more intense over the Indian Ocean than in the control run (Figure 18(b)). Its vertical and horizontal structures are quite similar to those in the control run, as is the general rainfall pattern (not shown).

5.3. *Horizontal resolution*

When the parcel radius is reduced by a factor of two in both the zonal and meridional directions the LAM continues to generate a strong and regular MJO (Figure 18(c)), with similar vertical and horizontal structures (not shown). The MJO is a little faster in this case (8 m s^{-1}), as it is in the case with zonally symmetric SST forcing (Figure 15). One feature both of these simulations share in common is a more narrow, equatorially confined band of heavy rainfall (not shown) than that in the control run.

To verify that the change in MJO speed is more a consequence of the change in basic-state precipitation structure than resolution, we repeated the higher resolution simulation making two changes: (i) reducing the mixing parameter, which leads to a less equatorially confined region of heavy rainfall, and (ii) enhancing rain evaporation, which helps to maintain a strong and regular MJO in weaker mixing regimes (case 4 in Table 3). These changes do indeed slow the MJO (Figure 18(d)), without changing its structure much, and also produce a less equatorially confined band of rainfall (not shown), which is more like that in the control run and in the observations.

We performed one more simulation with the new parameters, this time with four times the horizontal resolution used in the control run (i.e. so that parcels are 16 times less massive). The MJO maintains its slow propogation speed, but exhibits much more of a hierarchical structure with embedded higher-frequency westward and eastward moving disturbances (Figure 19(a)). Composite MJO structure (e.g. Figure 19(b)–(d)) is similar to that in the previous case and in the control run, and there continues to be a relatively broad region of heavy rainfall over the Indian Ocean and West Pacific (not shown). One aspect of the MJO that improves at this relatively high resolution, is that the low-level moistening ahead of the MJO becomes deeper (Figure 19(c)), which might be a consequence of higher frequency disturbances embedded within the MJO.

Overall, the numerical sensitivity tests reveal that the MJOs simulated with the LAM are only weakly sensitive to changes in time step, vertical resolution and horizontal resolution. Moreover, some of the changes that are evident, such as an increase in MJO

© 2013 Royal Meteorological Society

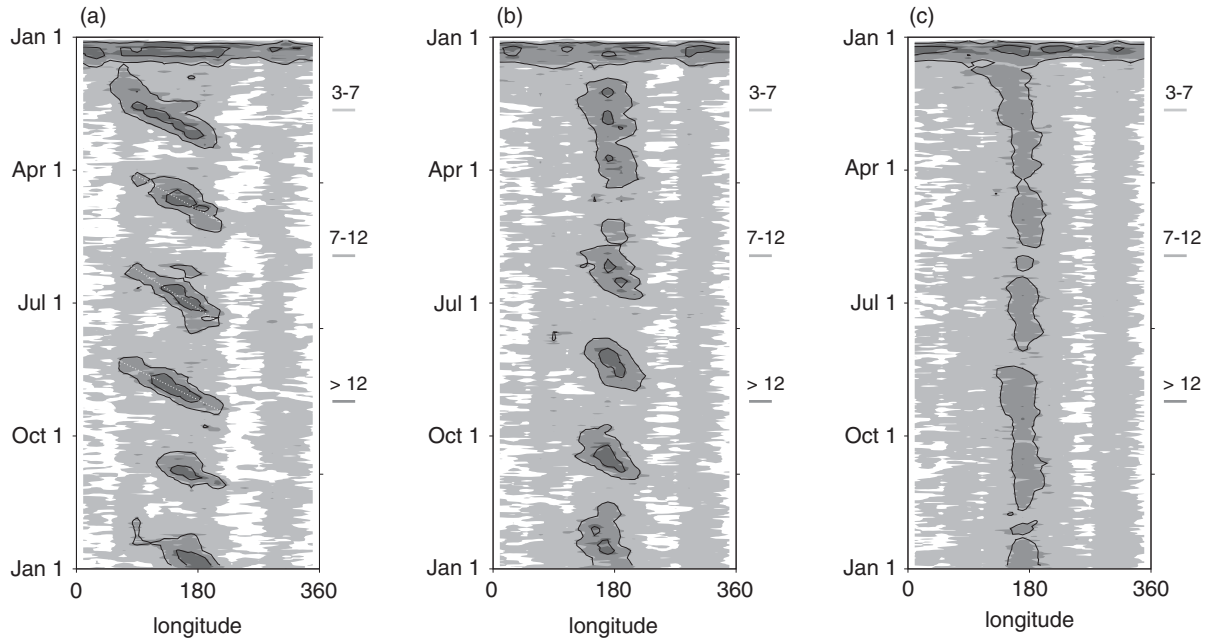

Figure 14. Time–longitude series of rainfall (mm day^{-1}) for Lagrangian atmospheric model simulations with convective mixing reduced to (a) 17×10^{-6} hPa^{-1}, (b) 12×10^{-6} hPa^{-1} and (c) 7×10^{-6} hPa^{-1}.

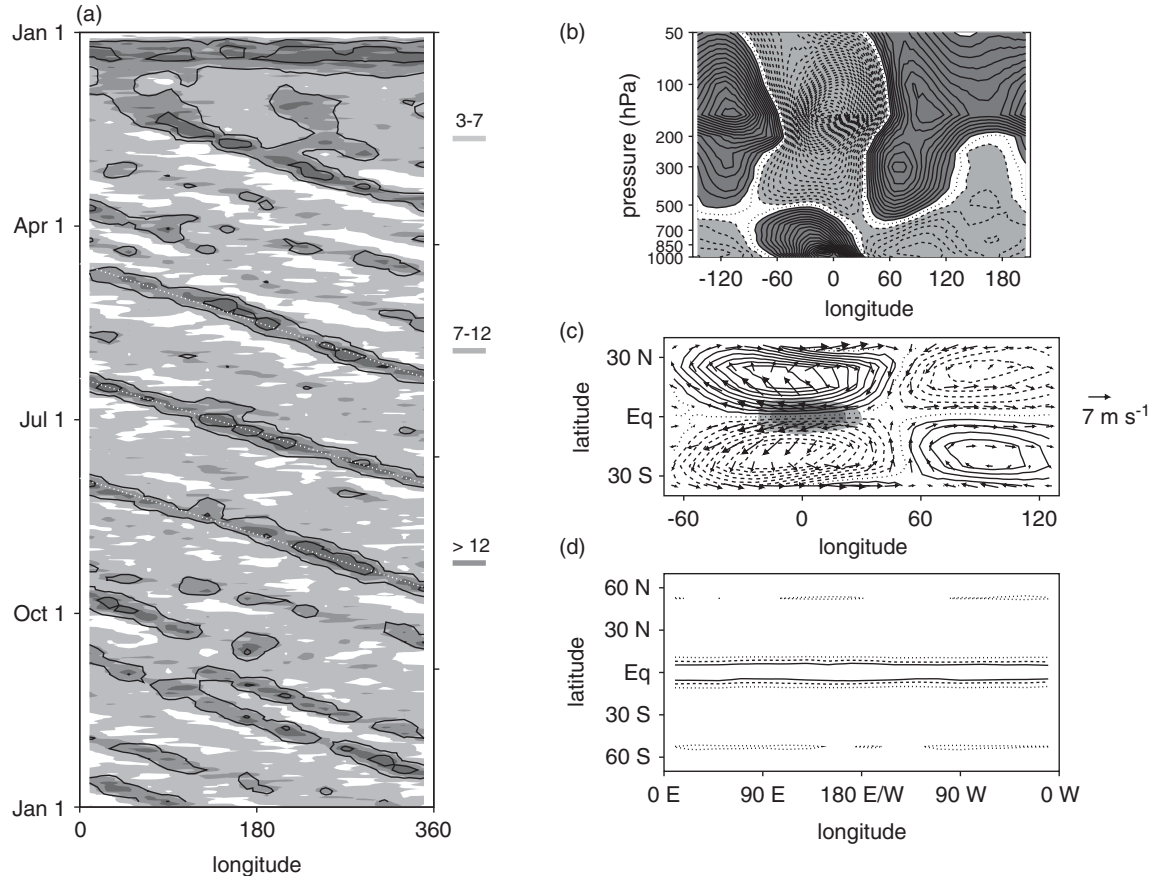

Figure 15. A simulation with zonally symmetric sea-surface temperature. (a) Rainfall time series (mm day^{-1}), with the approximate path of a strong Madden–Julian Oscillation (MJO) marked with a dotted line. (b) Composite MJO zonal wind perturbation (0.5 m s^{-1}). (c) Composite MJO 200 hPa flow (10^6 m^{2}s^{-1} contour interval). (d) Average rainfall for days 100–365 (3, 5 and 7 mm day^{-1} contours are dotted, dashed and solid respectively).

propagation speed in one higher resolution run, seem to be more a consequence of changes in the average precipitation pattern than a direct numerical effect. Finally, even when parcels are much smaller than in the control run (Figure 19), the gross structure of the MJO is the same, which is further evidence that the essence of the MJO in the LAM is a coupling between large-scale circulations and the GLO convective parametrization, with synoptic-scale convective disturbances contributing only secondary details to vertical structure.

6. The MJO and equatorial super rotation

Through the process of carrying out the many simulations required to tune the LAM and to test numerical and physical sensitivities, one point became quite clear: there is a strong correlation between MJO activity and equatorial super rotation in the LAM. For a given model resolution and configuration, when parameters are tuned to generate a stronger MJO (e.g. the mixing parameter is increased), westerlies develop and/or intensify in the

© 2013 Royal Meteorological Society

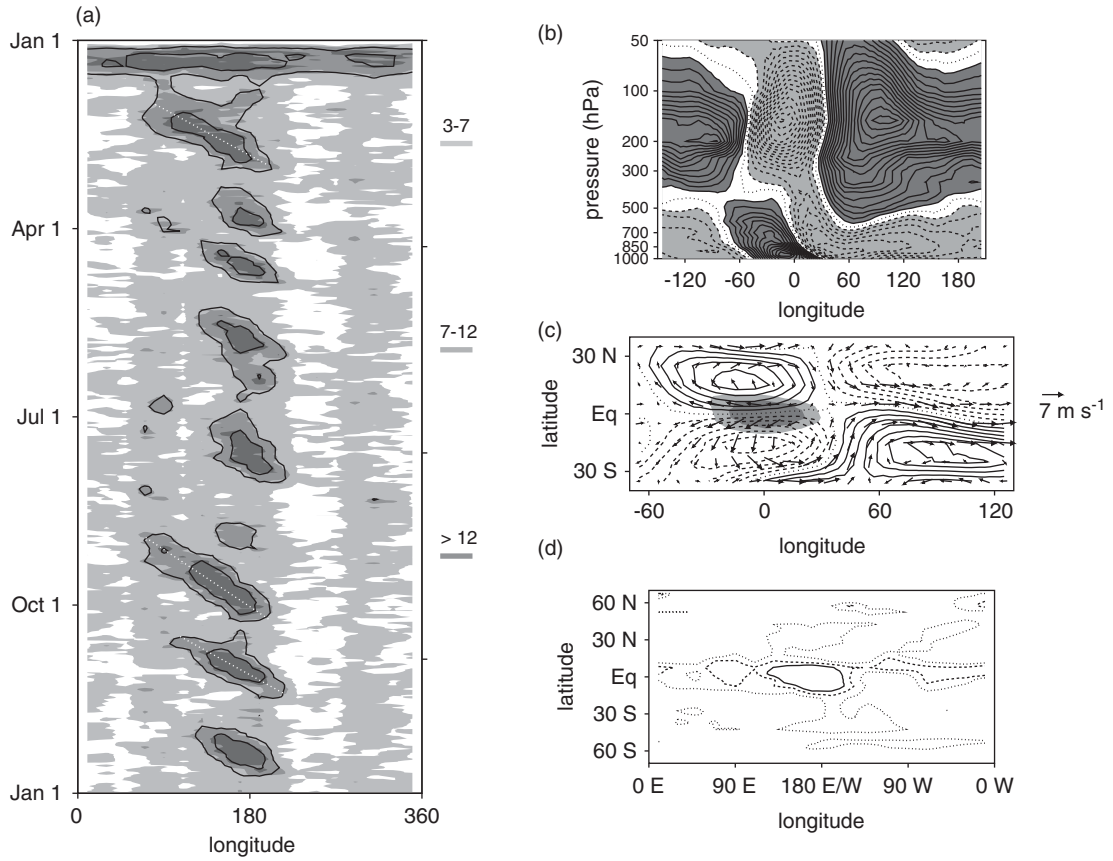

Figure 16. A simulation with a moisture independent radiative scheme (a) Rainfall time series (mm day^{-1}), with the approximate paths of three strong Madden–Julian Oscillations (MJOs) marked with dotted lines. (b) Composite MJO zonal wind perturbation (0.5 m s^{-1}). (c) Composite MJO 200 hPa flow (10^6 m^{2}s^{-1} contour interval). (d) Average rainfall for days 100–365 (3, 5 and 7 mm day^{-1} contours are dotted, dashed and solid respectively).

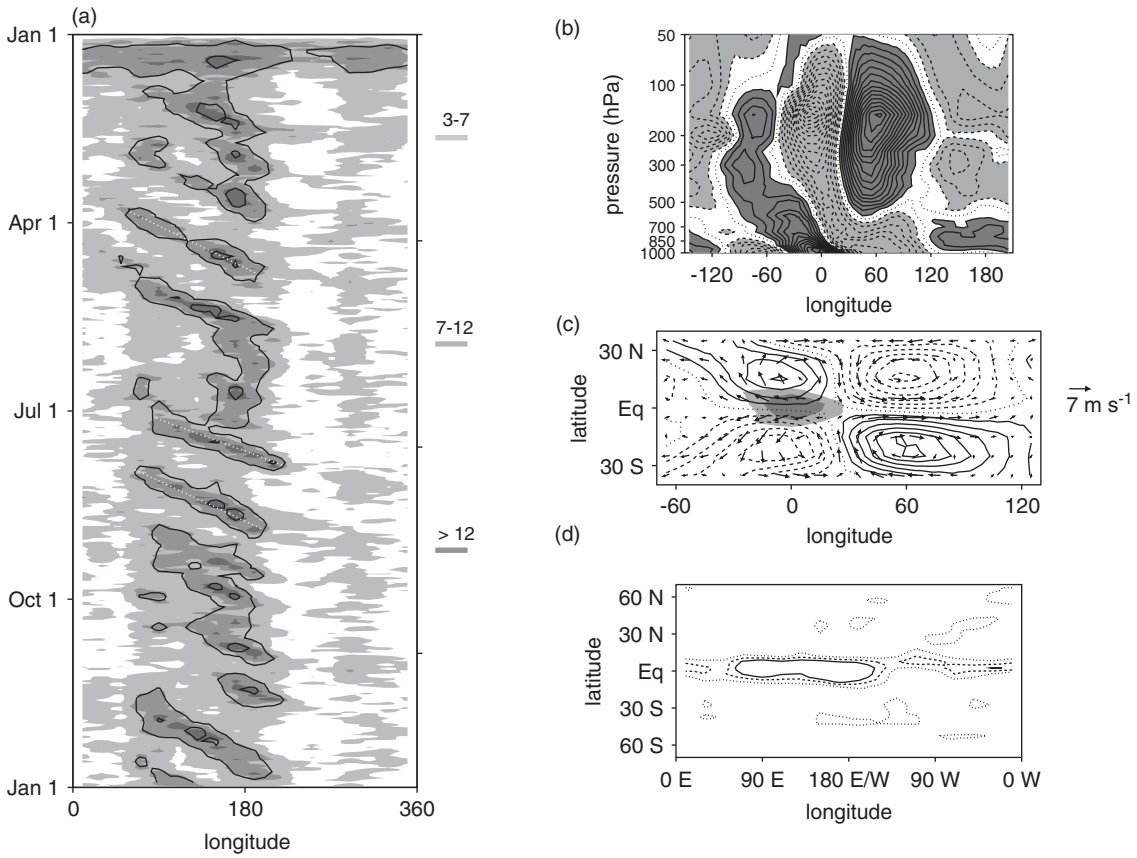

Figure 17. A simulation with wind-independent surface heat fluxes. (a) Rainfall time series (mm day^{-1}), with the approximate path of several strong Madden–Julian Oscillations (MJOs) marked with dotted lines. (b) Composite MJO zonal wind perturbation (0.5 m s^{-1}). (c) Composite MJO 200 hPa flow (10^6 m^{2}s^{-1} contour interval). (d) Average rainfall for days 100–365 (3, 5 and 7 mm day^{-1} contours are dotted, dashed and solid respectively).

© 2013 Royal Meteorological Society

Table 3. Model parameters for numerical sensitivity tests.

Run	Parcels (Pa^{-1})	Columns	Mixing (Pa^{-1})	Evaporation (Pa^{-1})	Time step (s)
1	$30^\circ \times 15^\circ \times 6.5$	$20^\circ \times 5^\circ$	21×10^{-6}	12×10^{-6}	2400, 1200
2	$30^\circ \times 15^\circ \times 9.3$	$20^\circ \times 5^\circ$	21×10^{-6}	12×10^{-6}	240
3	$15^\circ \times 7.5^\circ \times 6.5$	$10^\circ \times 2.5^\circ$	21×10^{-6}	12×10^{-6}	2400
4	$15^\circ \times 7.5^\circ \times 6.5$	$10^\circ \times 2.5^\circ$	17×10^{-6}	17×10^{-6}	2400
5	$7.5^\circ \times 3.75^\circ \times 6.5$	$5^\circ \times 1.25^\circ$	17×10^{-6}	17×10^{-6}	1200

upper troposphere over the Equator (e.g. Figure 20(a)–(c)). This super rotation is weaker in higher resolution simulations with MJOs (e.g. Figure 20(d)), and it vanishes in higher resolution simulations without MJOs. The super rotation is mostly confined to the upper troposphere, with minimal changes in lower tropospheric winds even when MJO activity changes drastically (e.g. Figure 20(a)–(c)).

Although rigorously explaining the nature and cause of this super rotation is beyond the scope of this article, we do mention several possible factors. First, as is evident by inspection of

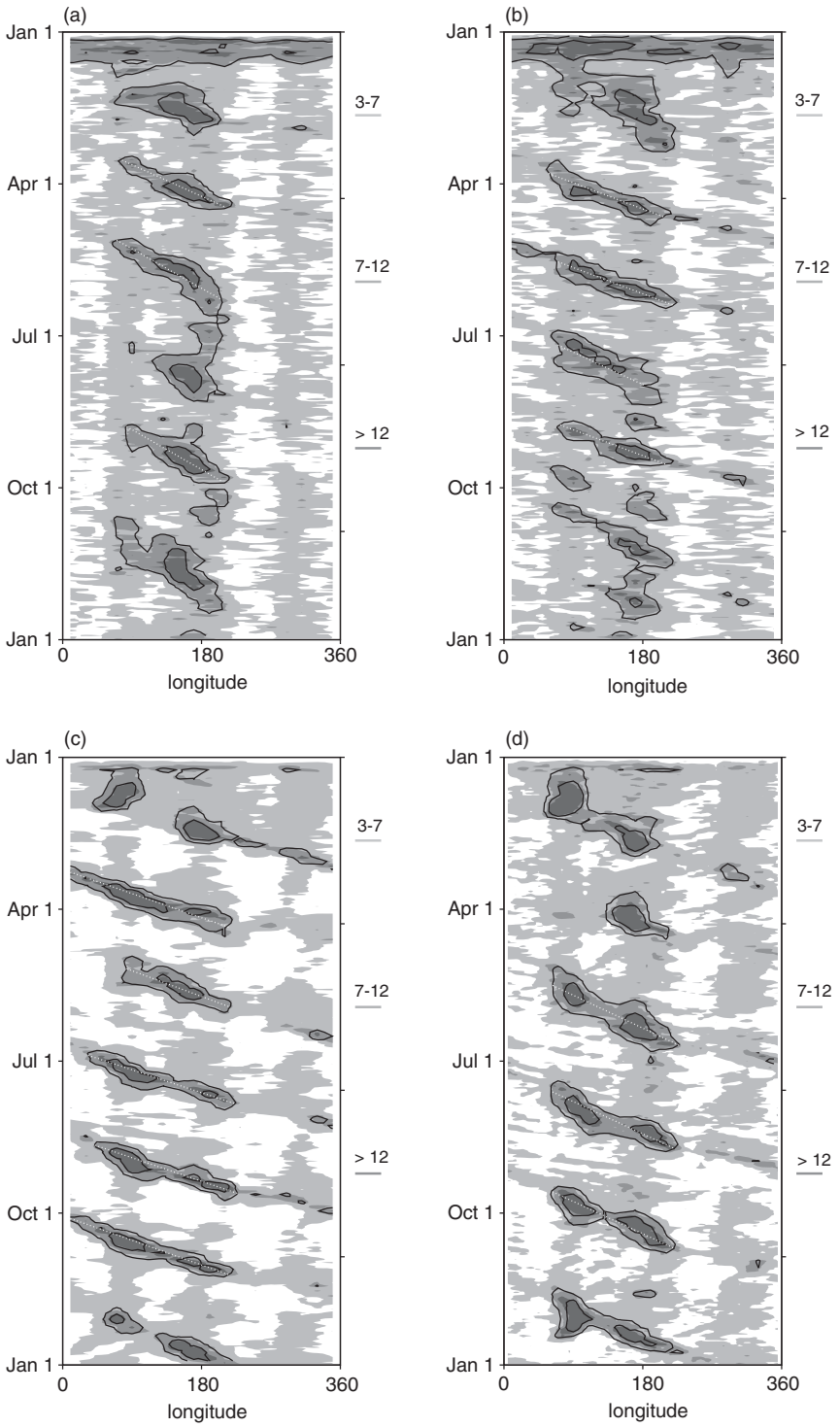

Figure 18. Rainfall time series for numerical sensitivity tests. (a) Reduced time step for column physics (e.g. global Lagrangian overturning, microphysics, radiation). (b) Increased parcel vertical thickness. (c) Doubled horizontal resolution. (d) Doubled horizontal resolution, reduced mixing and enhanced evaporation.

© 2013 Royal Meteorological Society

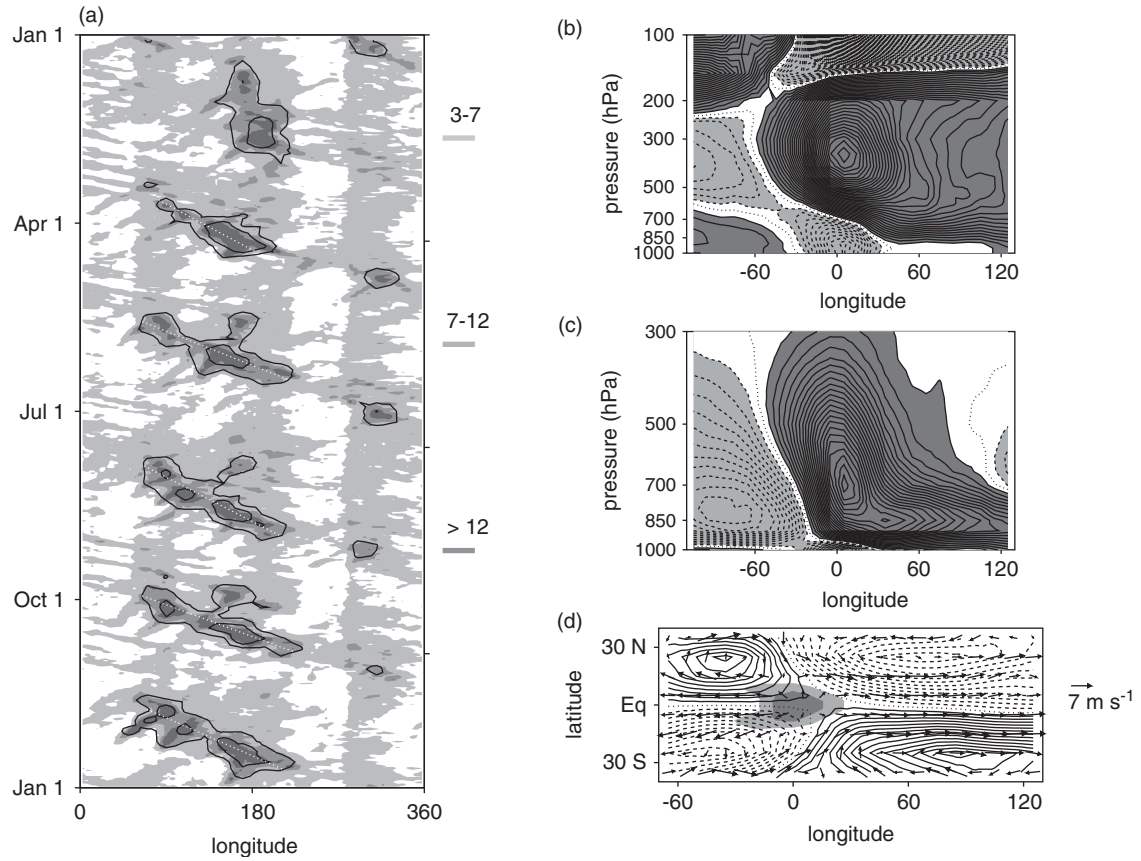

Figure 19. A simulation with four times the horizontal resolution of the control run, reduced mixing and enhanced evaporation. (a) Rainfall time series (mm day^{-1}), with the approximate path of strong Madden–Julian Oscillations (MJOs) marked with dotted lines, and contours of low-pass filtered rainfall shown for 7 and 12 mm day^{-1}. (b) Composite MJO potential temperature perturbation (0.1 K). (c) Composite MJO specific humidity perturbation (0.1 g kg^{-1}). (d) Composite MJO 200 hPa flow (10^6 m^{2}s^{-1} contour interval).

the MJO 200 hPa quadrapole gyre (e.g. Figure 10(a)) there is a positive correlation between westerlies (easterlies) and flow towards (away from) the Equator, suggesting that the MJO's perturbation flow contributes to upper-level equatorial super rotation. Second, as noted by Kraucunas and Hartmann (2005), upper-level equatorial easterlies become stronger when tropical heating moves off the Equator, and many of our simulations with weaker MJOs produce more off-equatorial tropical rainfall (not shown). Third, it is possible that there is some aspect of momentum transport unique to the Lagrangian framework or the GLO parametrization that simultaneously enhances both the MJO and equatorial super rotation.

7. Summary

In this study we show that a novel Lagrangian atmospheric model can generate surprisingly realistic MJOs, even at very low resolution. The model employs a unique convective parametrization (GLO), in which air parcels exchange vertical positions in convectively unstable regions. When a sufficient amount of mixing is prescribed between adjacent ascending and descending parcels, strong MJOs spontaneously form that are robust to changes in model resolution and variations in column physics, and which are relatively weakly sensitive to changes in rainfall evaporation.

Experiments aimed at characterizing the general behaviour of MJOs simulated with the LAM reveal the following: (i) mixing between parcels ascending and descending in convective regions is a key process for generating MJOs; (ii) MJO-like disturbances develop when zonally symmetric SSTs are prescribed, which propagate slightly faster than observed MJOs; (iii) in general, the faster MJOs propagate the more average rainfall is confined to the equatorial region; (iv) MJOs develop even when radiation is insensitive to variations in water vapour, although they appear to be less frequent in that case; (v) MJOs can develop with wind-independent surface heat fluxes, and there is a preference for wavenumber 2 structure in that case; (vi) there is a strong correlation between MJO activity and equatorial super rotation in the upper troposphere; and (vii) the essence of the MJO is a coupling between large-scale circulations and physics captured by the GLO parametrization.

In order to better undertand the MJO's eastward propagation and scale selection in the LAM, we examine composite plots of vertical motion and low-level moisture advection (Figure 21).

There are subsidence perturbations along the Equator both to the east and to the west of the MJO's precipitation centre (Figure 21(a)). The subsidence to the west covers a slightly larger area, and is slightly more intense. It probably plays a role in the rapid drying on the western edge of the MJO (e.g. Figure 8). However, there is a more dramatic east–west asymmetry in how low-level meridional flow advects moisture. In Figure 21(b) and (c) we plot composite MJO 850 hPa flow perturbations along with contours of the time-mean 700–1000 hPa moisture field, for both the control case and the run with zonally symmetric SSTs. In both cases, meridional flow advects drier air into the western edge of the MJO precipitation region. In contrast, to the east of the precipitation centre the flow either runs parallel to moisture contours or advects moisture slightly poleward (Figure 21(b) and (c)). For the run with zonally symmetric SSTs, in which rainfall is more confined to equatorial regions (Figure 15(d)), there is a stronger meridional moisture gradient (Figure 21(c)), which equates to more rapid drying on the western edge of the MJO, and which probably plays a role in the MJO's more rapid propagation in this case. The meridional extent of moisture also seems to be related to the scale selection of the MJO; LAM runs with narrow equatorial rainfall bands also have a more prominant zonal wavenumber 2 component to both precipitation and flow fields (e.g. Figures 15 and 17).

© 2013 Royal Meteorological Society

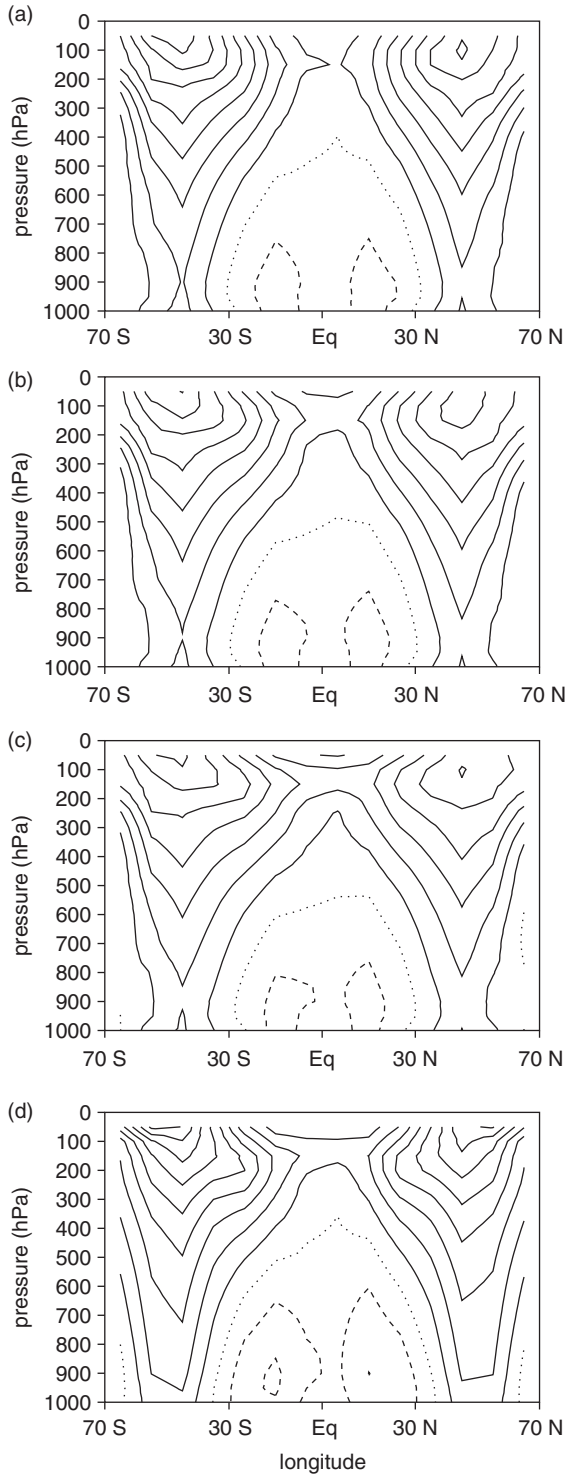

Figure 20. Equatorial super rotation and its dependence on mixing and resolution. ((a)–(c)) Average zonal winds for low-resolution runs with mixing parameters of 7, 12 and 17 $\times$ 10^6 Pa^{-1}. (d) Zonal average zonal winds for the highest resolution run (shown in Figure 19). Note that upper tropospheric equatorial super rotation increases with increasing mixing (and stronger Madden–Julian Oscillations; MJOs) for a given model resolution as shown by (a)–(c). Equatorial super rotation is weaker for higher resolution runs, even with strong MJOs, as is shown by (d).

One intriguing aspect of the LAM's success at simulating MJOs and tropical rainfall patterns in general, is that its air parcels are orders of magnitude larger than convective plumes in nature. This result is not as surprising when the following points are kept in mind. First, unlike a cloud-resolving model, the LAM does not calculate three-dimensional flow fields around an air parcel in order to determine its vertical motion. Rather, the buoyancy of a parcel relative to its environment determines whether it becomes part of a convective plume (under GLO) and, if it does, the vertical extent of its transport. Ultimately, the same constraints hold for air parcels in cloud-resolving models and in nature. Second, the vertical transport associated with a single parcel in the LAM represents the combined effects of many convective plumes in nature. As long as the sample of parcels in a modelled convective system is sufficiently large to be representative of those in an observed system, there is no need to simulate the behaviour of every single parcel – much like a poll can predict the outcome of an election if its sample is sufficiently large and representative of the electorate. The fact that higher resolution MJO simulations produce the same gross MJO structure and behaviour as the control run suggests that the latter has a sufficiently large sample of air parcels for simulating the MJO. Finally, it is apparently only necessary to capture the gross or net effects of mixing between updrafts and downdrafts and evaporation in order to simulate the MJO. By incorporating these processes in a simple way, with a single constant determining the magnitude of each, it is relatively straightforward to tune the LAM to achieve bulk effects like those that occur in nature, by comparing modelled and observed precipitation patterns, temperature and moisture profiles and convective system behaviour. It also helps that the modelled mixing and evaporation are prescribed in terms of parcel-ascent distances and raindrop-fall distances, which makes them only weakly sensitive to the model's time step and vertical resolution.

Despite the simplicity of the LAM's equations of motion and physical parametrizations, it is not obvious why the model simulates more realistic MJOs than are typically found in conventional climate models. We suspect that much of this success stems from the use of the GLO convective parametrization, which seems to mimic the vertical transports of convecting parcels in nature despite the extremely large size of model parcels. In particular, the existence and depth of convective updrafts are controlled by parcel buoyancy, and there is a straightforward way to model mixing between ascending and descending parcels and the evaporation of rainfall. Moreover, the GLO parametrization simultaneously ties together multiple processes including deep moist convection, compensating subsidence dry convection (e.g. in the boundary layer) and the replacement of boundary-layer air that ascends in convective updrafts. The Lagrangian numerics may provide an additional advantage by eliminating spurious numerical mixing, which creates unknown and variable amounts of diffusion in Eulerian models (e.g. Griffies *et al.*, 2000). For this reason it may actually be easier to precisely set the amount of mixing between convective updrafts and downdrafts in an ultra-coarse resolution version of the LAM than in a cloud-resolving model. The Lagrangian treatment of advection also helps the LAM to simulate tight moisture gradients near the Equator and to accurately transport moisture over large distances.

Other recent studies have simulated key aspects of MJO structure using coarse-resolution, nonlinear models with simplified convective parametrizations. Majda and Stechmann (2011) were able to reproduce the MJO upper-level quadrapule vortex, slow eastward propagation and flat dispersion relation with a highly simplified 'skeleton' model that is mostly linear except for a single term that predicts the tendency of local convective activity. Khouider *et al.*(2011) used a more sophisticated multicloud parametrization coupled with a fully nonlinear dynamical core to study the organization of tropical convection. They found that they could switch between realistic convectively coupled wave regimes and MJO-like regimes by altering the moisture stratification and stratiform rain fraction. These studies along with the LAM simulations presented here suggest that the gross MJO structure can be obtained by coupling large-scale atmospheric motions to a simplified convective parametrization, without the need to simultaneously simulate synoptic-scale waves. Of course, including such waves can improve details of vertical structure, such as in the higher resolution simulation presented here (Figure 19).

Although this article provides several clues about what constitutes the most fundamental dynamics of the MJO in the

© 2013 Royal Meteorological Society

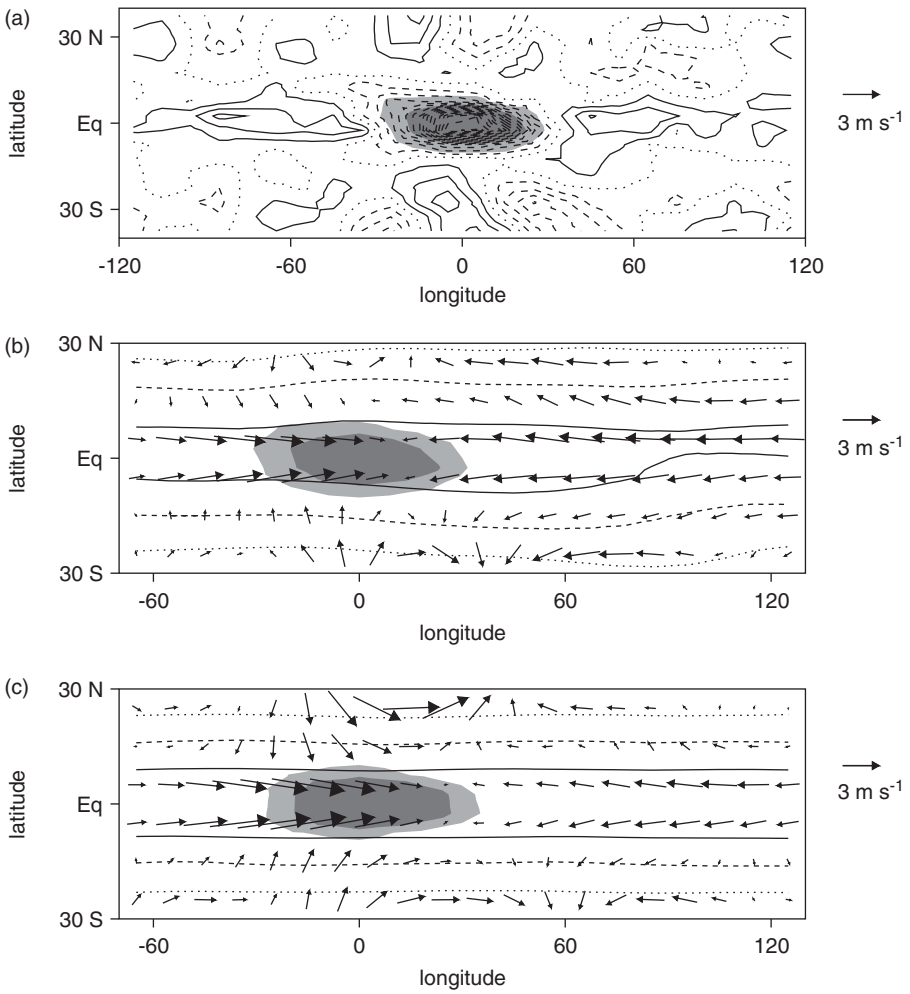

Figure 21. Potential factors contributing to the eastward propagation of the MJO. (a) Composite Madden–Julian Oscillations (MJO) 300–700 hPa vertical velocity for the control simulation (30 hPa day^{-1} contours). (b) Composite MJO 850 hPa flow superposed on time average 700–1000 hPa specific humidity field for the control simulation (7, 9 and 12 g kg^{-1} contours are dotted, dashed and solid lines respectively). (c) Same fields as in (b), but for the simulation with zonally symmetric SSTs. For the purpose of contructing (b) and (c) it is assumed that the MJO is centred on the Equator at 140°E . Regions of precipitation with values greater that 3 and 7 mm day^{-1} are shaded light and dark respectively in all panels.

LAM and possibly in nature, important questions remain that will require a parcel-based analysis and detailed moisture budget to fully answer, such as: (i) Why is including mixing between adjacent ascending and descending parcels the key to simulating a strong MJO? (ii) What causes the low-level moistening ahead of the MJO? (iii) What determines the MJO's period? We plan to address these questions in a sequel to this article, which will take advantage of the copious parcel information provided by the LAM.

Acknowledgement

We thank Dargen Frierson for suggesting the use of the new radiation scheme. We thank Raymond Shaw for advice on implementing cloud water into the microphysics. This research was supported by NSF Grant AGS-1116885. We thank two anonymous reviewers for their comments and suggestions.

References

Barrett BS, Leslie LM. 2009. Links between tropical cyclone activity and Madden–Julian Oscillation phase in the North Atlantic and northeast Pacific basins. *Mon. Weather Rev.* **137**: 727–744.

Blade I, Hartmann DL.1993. Tropical intraseasonal oscillations in a simple nonlinear model. *J. Atmos. Sci.* **50**: 2922–2939.

Caballero R, Huber M. 2010. Spontaneous transition to superrotation in warm climates simulated by CAM3 *Geophys. Res. Lett.* **37**: L11701, doi: 10.1029/2010GL043468.

Cassou C. 2008. Intraseasonal interaction between the Madden–Julian Oscillation and the North Atlantic Oscillation. *Nature* **455**: 523–527, doi: 10.1038/nature07286.

Ciesielski PE, Johnson RH, Haertel PT, Wang J. 2003. Corrected TOGA COARE sounding humidity data: impact on convection and climate. *J. Clim.* **16**: 2370–2384.

Emanuel KA. 1987. An air–sea interaction model of intraseasonal oscillations in the tropics. *J. Atmos. Sci.* **44**: 2324–2340.

Fedorov AV. 2002. The response of the coupled tropical ocean–atmosphere to westerly wind bursts. *Q. J. R. Meteorol. Soc.* **128**: 1–23.

Fedorov AV, Harper SL, Winter B, Wittenberg A. 2003. How predictable is El Nino? *Bull. Am. Meteorol. Soc.* **84**: 911–919.

Frierson DMW, Held IM, Zuria-Gotor P. 2006. A gray radiation aquaplanet moist GCM. Part I: static stability and eddy scale. *J. Atmos. Sci.* **63**: 2548–2566.

Grabowski WW. 2001. Coupling cloud processes with the large-scale dynamics using the cloud-resolving convection parameterization (CRCP). *J. Atmos. Sci.* **58**: 978–997.

Griffies SM, Pacanowski RC, Hallberg RW. 2000. Spurious diapycnal mixing associated with advection in a *z*-coordinate ocean model. *Mon. Weather Rev.* **128**: 538–567.

Haertel PT. 2012. A Lagrangian method for simulating geophysical fluids. In *Geophysical Monograph 200, Lagrangian Modeling of the Atmosphere*, Lin J, Brunner D, Gerbig C, Stohl A, Luhar A, Webley P. (eds.). American Geophysical Union: Washington, DC.

Haertel PT, Kiladis GN. 2004. Dynamics of two day equatorial waves. *J. Atmos. Sci.* **61**: 2707–2721.

Haertel PT, Randall DA. 2002. Could a pile of slippery sacks behave like an ocean? *Mon. Weather Rev.* **130**: 2975–2988.

Haertel P, Straub KH. 2010. Simulating convectively coupled Kelvin waves using Lagrangian overturning for a convective parameterization. *Q. J. R. Meteorol. Soc.* **136**: 1598–1613.

Haertel PT, Randall DA, Jensen TG. 2004. Simulating upwelling in a large lake using slippery sacks. *Mon. Weather Rev.* **132**: 66–77.

Haertel PT, Kiladis GN, Rickenbach T, Denno A. 2008. Vertical mode decompositions of 2-day waves and the Madden–Julian oscillation. *J. Atmos. Sci.* **65**: 813–833.

Haertel PT, Van Roekel L, Jensen T. 2009. Constructing an idealized model of the north Atlantic Ocean using slippery sacks. *Ocean Model.* **27**: 143–159.

© 2013 Royal Meteorological Society

Hendon HH, Liebmann B. 1994. Organization of convection within the Madden–Julian oscillation. *J. Geophys. Res.* **99**: 8073–8083, doi: 10.1029/94JD00045.
Houze RA Jr., Chen SS, Kinsmill DE, Serra Y, Yuter SE. 2000. Convection over the Pacific warm pool in relation to the atmospheric Kelvin–Rossby wave. *J. Atmos. Sci.* **57**: 3058–3089.
Huffman GJ, Adler RF, Morrissey MM, Bolvin DT, Curtis S, Joyce R, McGavock B, Susskind J. 2001. Global precipitation at one-degree daily resolution from multisatellite observations. *J. Hydrometeor.* **2**: 36–50.
Kessler WS. 2001. EOF representations of the Madden–Julian Oscillation and its connection with ENSO. *J. Clim.* **14**: 3055–3061.
Kessler WS, Kleeman R .2000. Rectification of the Madden–Julian Oscillation into the ENSO cycle. *J. Clim.* **13**: 3560–3575.
Khairoutdinov MF, Randall DA. 2001. A cloud-resolving model as a cloud parameterization in the NCAR community climate system model: preliminary results. *Geophys. Res. Lett.* **28**: 3617–3620, doi: 10.1029/2001GL013552.
Khouider B, St-Cyr A, Majda AJ, Tribbia J. 2011. The MJO and convectively coupled waves in a course-resolution GCM with a simple multicloud parameterization. *J. Atmos. Sci.* **68**: 240–264.
Kiladis GN, Straub KH, Haertel PT. 2005. Zonal and vertical structure of the Madden–Julian oscillation. *J. Atmos. Sci.* **62**: 2790–2809.
Kim D, Sobel AH, Maloney ED, Frierson DMW, Kang IS. 2011. A systematic relationship between intraseasonal variability and mean state bias in AGCM simulations. *J. Clim.* **24**: 5506–5520.
Kraucunas I, Hartmann DL. 2005. Equatorial superrotation and the factors controlling the zonal-mean zonal winds in the tropical upper troposphere. *J. Atmos. Sci.* **62**: 371–389.
Lau KM, Peng L. 1987. Origin of low-frequency (intraseasonal) oscillations in the tropical atmosphere. Part I: basic theory. *J. Atmos. Sci.* **44**: 950–972.
L'Ecuyer TS, McGarragh G. 2010. A 10-year climatology of tropical radiative heating and its vertical structure from TRMM observations. *J. Clim.* **23**: 519–541.
Lin X, Johnson RH. 1996. Kinematic and thermodynamic characteristics of the flow over the western Pacific warm pool during TOGA COARE. *J. Atmos. Sci.* **53**: 695–715.
Lin JL, Zhang M, Mapes B. 2005. Zonal momentum budget of the Madden–Julian Oscillation: the source and strength of equivalent linear damping. *J. Atmos. Sci.* **62**: 2172–2188.
Lin JL, Kiladis GN, Mapes BE, Weickmann KM, Sperber KR, Lin W, Wheeler MC, Schubert SD, Genio AD, Donner LJ, Emori S, Gueremy J-F, Hourdin F, Rasch PJ, Roeckner E, Scinocca JF. 2006. Tropical intraseasonal variability in 14 IPCC AR4 climate models. Part I: convective signals. *J. Clim.* **19**: 2665–2690.
Lorenz DJ, Hartmann DL. 2006. The effect of the MJO on the North American monsoon. *J. Clim.* **19**: 333–343.
Madden R, Julian P. 1971. Detection of a 40–50 day oscillation in the zonal wind in the tropical pacific. *J. Atmos. Sci.* **702**: 702–708.
Madden R, Julian P. 1972. Description of global-scale circulation cells in the tropics with a 40–50 day period. *J. Atmos. Sci.* **29**: 1109–1123.
Madden RA, Julian PR. 1994. Observations of the 40–50 day tropical oscillation – a review. *Mon. Weather Rev.* **122**: 814–837.
Majda AJ, Biello JA. 2004. A multiscale model for tropical intraseasonal oscillations. *Proc. Natl. Acad. Sci.* **101**: 4736–4741.
Majda AJ, Stechmann SN. 2009. The skeleton of tropical intraseasonal oscillations. *Proc. Natl. Acad. Sci.* **106**: 8417–8422.
Majda AJ, Stechmann SN. 2011. Nonlinear dynamics and regional variations in the MJO skeleton. *J. Atmos. Sci.* **68**: 3053–3071.
Maloney ED, Hartmann DL. 2000. Modulation of hurricane activity in the Gulf of Mexico by the Madden–Julian Oscillation. *Science* **287**: 2002–2004.
Moncrieff MW. 2004. Analytic representation of the large-scale organization of tropical convection. *J. Atmos. Sci.* **61**: 1521–1538.
Nakazawa T. 1988. Tropical super clusters within intraseasonal variations over the western Pacific. *J. Meteorol. Soc. Jpn.* **66**: 823–839.
Neale RB, Hoskins BJ. 2000. A standard test for AGCMs including their physical parameterizations: I: the proposal? *Atmos. Sci. Lett.* **1**: 101–107.
Raymond DJ. 2001. A new model of the Madden–Julian oscillation. *J. Atmos. Sci.* **58**: 2807–2819.
Sobel A, Maloney E. 2012. An idealized semi-empirical framework for modeling the Madden–Julian oscillation. *J. Atmos. Sci.* **69**: 1691–1705.
Thayer-Calder K, Randall DA. 2009. The role of convective moistening in the Madden–Julian oscillation. *J. Atmos. Sci.* **66**: 3297–3312.
Vecchi GA, Bond NA. 2003. The Madden–Julian Oscillation (MJO) and northern high latitude wintertime surface air temperatures. *Geophys. Res. Lett.* **31**: LO4104, doi: 10.1029/2003GL018645.
Wang B. 2005. *Theory, in Intraseasonal Variability in the Atmosphere–Ocean Climate System*, Chapter 10, Lau WKM, Waliser D. (eds.): 307–351 Springer: New York, NY.
Wang B, Rui H. 1990. Dynamics of the coupled moist Kelvin–Rossby wave on an equatorial plane. *J. Atmos. Sci.* **47**: 397–413.
Weickmann KM, Lussky GR, Kutzbach JE. 1985. Intraseasonal (30–60 day) fluctuations of outgoing longwave radiation and 250 mb streamfunction during northern winter. *Mon. Weather Rev.* **113**: 941–961.
Wu MLC, Schubert S, Huang NE. 1999. The development of the South Asian summer monsoon and the intraseasonal oscillation. *J. Clim.* **12**: 2054–2075.
Zhang C. 2005. Madden–Julian Oscillation. *Rev. Geophys.* **43**: RG2003 36 pp, doi: 10.1029/2004RG000158.

© 2013 Royal Meteorological Society